

Improving the Seismic Performance of Structural Steel Systems Through Advanced Testing

James Ricles^(⊠)

□

Lehigh University, Bethlehem, PA 18015, USA jmr5@lehigh.edu

Abstract. Recent earthquakes in many parts of the world have resulted in damage to the civil infrastructure, resulting in fatalities and economic loss. This experience has resulted in stake holders demanding a more resilient infrastructure and the mitigation of earthquake hazards to minimize their impact on society. Researchers have developed concepts for structural steel systems to promote resilient performance. Real-time hybrid simulation (RTHS) provides an experimental technique to meet the need to validate new concepts. RTHS enables a complete structural system, including the soil and foundation to be considered in a simulation, interaction effects and rate dependency in component and system response to be accounted for, and realistic demand imposed onto the system for prescribed hazard levels. This paper presents the concept of RTHS and developments achieved at the Lehigh NHERI Experimental Facility that have advanced RTHS to enable accurate large-scale, multidirectional simulations involving multi-natural hazards to be performed. The role that hybrid simulation has played in these developments and how its use has enabled a deeper understanding of structural system behavior under seismic and wind loading will be discussed. Examples include self-centering steel moment resisting frame systems, braced frame systems with nonlinear viscous, and tall buildings with outriggers that are outfitted with nonlinear viscous.

Keywords: Real-time hybrid simulation · Multi-hazards · Advanced multi-directional testing · Resiliency · Unconditional stable dissipative direct integration algorithms

1 Introduction

Recent earthquakes in many parts of the world have resulted in damage to the civil infrastructure, resulting in fatalities and economic loss [1–5]. This experience has resulted in stake holders demanding a more resilient infrastructure and the mitigation of earthquake hazards to minimize the impact of their occurrence on society [6]. Consequently, numerous researchers have developed concepts to promote resilient performance structural systems, including those constructed from structural steel. The incorporation of the outcomes of this research into practice requires a performance-based design framework that can be readily incorporated into codes and used by design engineers. To develop this framework, experimental and numerical studies are needed

to validate design procedures and their ability to enable a structural system to achieve resiliency for prescribed hazard levels.

Numerical studies may be inaccurate when good computational models for components of the system do not exist. Real-time hybrid simulation (RTHS) offers an experimental technique to meet the need to validate new concepts, while overcoming computational modelling burdens. In a hybrid simulation, components of a system for which accurate computational models are not available are physically modelled in the laboratory as experimental substructures, and kinematically linked to an analytical substructure. The remaining part of the system not included in the experimental substructure, and for which accurate computational models exists, are part of the analytical substructure. The analytical substructure is formed using available accurate computational models. RTHS enables a complete structural system, including the soil and foundation, to be considered in a simulation in addition to interaction effects and rate dependency in component and system response to be accounted for. Realistic demand can be prescribed and imposed onto the system for various hazard levels. In addition, the physical component of the system that is tested in the laboratory, namely the experimental substructure, is kinematically linked to the analytical substructure allowing the interaction effects of the structural system with the experimental substructure to be accounted for.

This paper presents the concept of RTHS and developments at the NHERI Lehigh Experimental Facility that have advanced this technique to enable accurate large-scale, multidirectional earthquake simulations to be performed. Structural system concepts that have been developed for achieving resilient response of structural steel systems to earthquake will be presented. The role that hybrid simulation has played in these developments and how its use has enabled a deeper understanding of structural system behaviour under seismic loading will be discussed. Examples include self-centering steel moment resisting frame systems; braced frame systems with nonlinear viscous dampers; along with tall buildings with outriggers systems outfitted with nonlinear viscous subjected to earthquakes.

2 Real-Time Hybrid Simulation Background

Real time hybrid simulation (RTHS) is a testing methodology where the complete structural system is represented in an experiment, though only a portion of it is physically present during the test. The first real-time hybrid simulation was performed by Nakashima et al. [7]. As shown Fig. 1, and introduced above, the structural system is divided into analytical and experimental substructures. Components of the system for which analytical models exist are modelled numerically and reside in the analytical substructure. The experimental substructure is comprised of the remaining components of the system, which are modelled physically in the laboratory. The mass and inherent viscous damping of the structural system are included in the analytical substructure.

The displacement compatibility between analytical and experimental substructures are enforced through their common degrees of freedom in real time to capture both the rate dependency of the experimental substructure and the real time response of the complete structural system. The equations of motion at time step i + 1 are shown

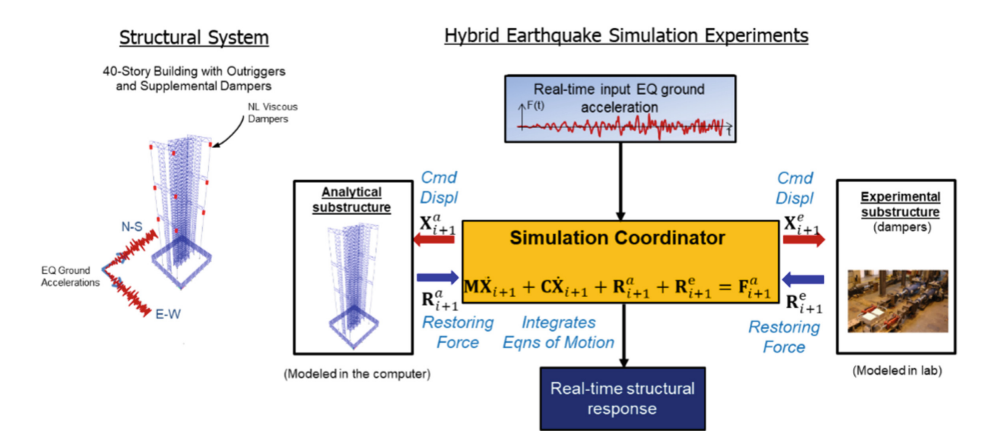


Fig. 1. Conceptual framework of a real-time hybrid simulation of a tall building with nonlinear viscous dampers.

below in Eq. (1), which includes the following terms: inertia $(M\ddot{X}_{i+1})$, inherent viscous damping $(C\dot{X}_{i+1})$, the restoring forces R_{i+1}^a and R_{i+1}^e of the analytical and experimental substructures, respectively, and the applied load F_{i+1} . The equations are numerically integrated to obtain displacements, velocities, and accelerations at each time step. These values are then used to compute the inertia, inherent viscous damping, and the restoring forces R_{i+1}^a of the analytical substructure. Simultaneously, the displacements associated with the experimental substructure (called the target displacements) are imposed onto this substructure, and the restoring forces R_{i+1}^e are measured. With the restoring forces for the analytical and experimental substructures known, the process is repeated for the next time step. Further details are given below in Sect. 2.1.

$$M\ddot{X}_{i+1} + C\dot{X}_{i+1} + R_{i+1}^a + R_{i+1}^e = F_{i+1}$$
 (1)

There are several challenges in performing a RTHS. These include: (1) integrating the equations of motion in real-time to determine the target displacements \mathbf{x}^t for the system; (2) performing the state-determination process in real-time to obtain the restoring forces \mathbf{R}^a_{i+1} , where often nonlinear computational models of the analytical substructure are required; and (3) accurate real-time control of the servo-hydraulic actuators used to impose command displacements \mathbf{x}^c in order that the target displacements \mathbf{x}^t are achieved and precise values of \mathbf{R}^e_{i+1} are obtained. These challenges are discussed further below and solutions to overcome the barriers that they pose are provided.

2.1 Integration of the Equations of Motion

Direct integration algorithms can broadly be classified into two types, namely, explicit and implicit [8]. Unlike the implicit schemes, a key advantage of explicit schemes is that they do not require any iteration. In an RTHS, such iterations may introduce undesired hysteresis because of loading and unloading during iteration within the time

step. While explicit schemes are preferred in RTHS they are generally only conditionally stable and therefore require that the integration time-step size be inversely proportional to the highest natural frequency present in the system. Consequently, for RTHS of structures with a large number of degrees of freedom (DOFs) explicit integration algorithms can require an unrealistically small time step. A small time step may not be viable to use for several reasons, including that the numerical computations for each time step must be completed in real-time within the step size.

Kolay and Ricles [8–10] proposed a family of model-based second-order accurate explicit algorithms with controllable numerical energy dissipation referred to as the $KR-\alpha$ Method. They showed that the method is unconditionally stable for linear elastic and stiffness softening type nonlinear response. The following equations describe the algorithm for a nonlinear MDOF system:

$$\dot{X}_{i+1} = \dot{X}_i + \Delta t \alpha_1 \ddot{X}_i \tag{2}$$

$$X_{i+1} = X_i + \Delta t \dot{X}_i + \Delta t^2 \alpha_2 \ddot{X}_i \tag{3}$$

$$\mathbf{M}\widehat{\ddot{\mathbf{X}}}_{i+1} + \mathbf{C}\dot{\mathbf{X}}_{i+1-\alpha_f} + \mathbf{R}_{i+1-\alpha_f} = \mathbf{F}_{i+1-\alpha_f}$$

$$\tag{4}$$

In Eqs. (2) and (3) Δt is the time step, X_i , \dot{X}_i , and \ddot{X}_i are the vectors of displacement, velocity and acceleration, respectively, at time step i. α_1 and α_2 are matrices of model-based integration parameters that are defined later. Equation (4) is the weighted equations of motion [9], where

$$\widehat{\ddot{X}}_{i+1} = (\mathbf{I} - \boldsymbol{\alpha}_3)\ddot{X}_{i+1} + \boldsymbol{\alpha}_3\ddot{X}_i \tag{5a}$$

$$\dot{X}_{i+1-\alpha_f} = (1-\alpha_f)\dot{X}_{i+1} + \alpha_f \dot{X}_i \tag{5b}$$

$$X_{i+1-\alpha_f} = (1 - \alpha_f)X_{i+1} + \alpha_f X_i$$
 (5c)

$$\mathbf{F}_{i+1-\alpha_f} = (1 - \alpha_f)\mathbf{F}_{i+1} + \alpha_f \mathbf{F}_i \tag{5d}$$

In Eq. (4) the matrices M and C are the structural system's mass and inherent damping matrices. Equation (4) can be simplified in terms of its use in RTHS by substituting Eq. (5a) into (4), whereby

$$\widehat{\boldsymbol{M}}_{1}\ddot{\boldsymbol{X}}_{i+1} = \boldsymbol{F}_{i+1-\alpha_{f}} - \boldsymbol{R}_{i+1-\alpha_{f}} - \boldsymbol{C}\dot{\boldsymbol{X}}_{i+1-\alpha_{f}} - \widehat{\boldsymbol{M}}_{2}\ddot{\boldsymbol{X}}_{i}$$
(6)

where

$$\widehat{\boldsymbol{M}}_1 = \boldsymbol{M}(\boldsymbol{I} - \boldsymbol{\alpha}_3) \qquad \widehat{\boldsymbol{M}}_2 = \boldsymbol{M}\boldsymbol{\alpha}_3 \qquad (7a, b)$$

 $\mathbf{R}_{i+1-\alpha_f}$ in Eq. (6) is the weighted restoring force vector that is calculated using the generalized trapezoidal rule:

$$\mathbf{R}_{i+1-\alpha_f} = (1 - \alpha_f)\mathbf{R}_{i+1} + \alpha_f \mathbf{R}_i = (1 - \alpha_f)\mathbf{R}(\mathbf{X}_{i+1}, \dot{\mathbf{X}}_{i+1}) + \alpha_f \mathbf{R}(\mathbf{X}_i, \dot{\mathbf{X}}_i)$$
(8)

As mentioned earlier, part of the restoring forces in a RTHS is measured from the physical experimental substructure and added with that determined from the analytical substructure. Thus, for such applications, Eq. (8) can be rewritten as

$$\mathbf{R}_{i+1-\alpha_f} = (1 - \alpha_f)(\mathbf{R}_{i+1}^a + \mathbf{R}_{i+1}^e) + \alpha_f(\mathbf{R}_i^a + \mathbf{R}_i^e)$$
(9)

The initial acceleration \ddot{X}_0 is determined from Eq. (10):

$$\mathbf{M}\ddot{\mathbf{X}}_0 = \mathbf{F}_0 - C\dot{\mathbf{X}}_0 + K\mathbf{X}_0 \tag{10}$$

In the above, α_1 , α_2 , and α_3 are matrices of integration parameters of size $n \times n$, where n is the number of degrees of freedom in the system. The integration parameters are formulated [9, 10] such that the KR- α Method possesses numerical energy dissipation and dispersion characteristics of the generalized α -method [11], where

$$\mathbf{\alpha}_1 = \mathbf{\alpha}^{-1} M$$
, $\mathbf{\alpha}_2 = (\frac{1}{2} + \gamma) \mathbf{\alpha}_1$, $\mathbf{\alpha}_3 = \mathbf{\alpha}^{-1} [\alpha_m M + \alpha_f \gamma \Delta t C + \alpha_f \beta \Delta t^2 K]$ (11a, b, c)

where $\alpha = [M + \gamma \Delta t C + \beta \Delta t^2 K]$. The matrix K is the initial elastic stiffness matrix of the structural system. The quantities γ , β , α_f , and α_m are scalars that are related to each other:

$$\gamma = \frac{1}{2} - \alpha_m + \alpha_f \qquad \beta = \frac{1}{4} \left(1 - \alpha_m + \alpha_f \right)^2 \qquad (12a, b)$$

The parameters α_f and α_m are related to the high-frequency spectral radius ρ_{∞} as follows:

$$\alpha_f = \frac{\rho_{\infty}}{\rho_{\infty} + 1}$$
 $\alpha_m = \frac{2\rho_{\infty} - 1}{\rho_{\infty} + 1}$
(13a, b)

To improve the KR- α Method, Kolay and Ricles developed the Modified KR- α (MKR- α) Method [12]. The MKR- α Method has enhanced control of overshooting characteristics and optimal numerical dissipation and parameterization. These were achieved by replacing β (see Eq. (12b)) with

$$\beta = \frac{1}{2} \left(\gamma + \frac{1}{2} \right) \tag{14}$$

and α_m (see Eq. (13b) with

$$\alpha_m = \frac{2\rho_{\infty}^3 + \rho_{\infty}^2 - 1}{\rho_{\infty}^3 + \rho_{\infty}^2 + \rho_{\infty} + 1} \tag{15}$$

The KR- α and MKR- α Methods both have only one free parameter ρ_{∞} , which can vary in the range of $0 \le \rho_{\infty} \le 1$. The other parameters are determined using Eqs. (11) through (15). The parameter ρ_{∞} controls the amount of numerical energy dissipation,

where $\rho_{\infty}=1$ and 0 indicate zero and the maximum numerical energy dissipation, respectively.

Figures 2 and 3 show the relative period error (PE) and the equivalent damping ratio $(\overline{\xi})$ with omega, respectively, where $PE = \frac{\overline{T} - T}{T}$, $T = \frac{2\pi}{\omega}$, $\overline{T} = \frac{2\pi}{\overline{\omega}}$, $\overline{\omega} = \frac{\overline{\Omega}}{\Delta t}$, with $\overline{\Omega}$ and $\overline{\xi}$ determined from Eq. (16) below.

$$\overline{\xi} = \frac{1}{2\overline{\Omega}} \ln(\sigma^2 + \varepsilon^2) \qquad \overline{\Omega} = \frac{\tan^{-1}(\varepsilon/\sigma)}{\sqrt{1 - \overline{\xi}^2}}$$
 (16)

In Eq. (16) σ and ε are the real and imaginary values of the principal roots of the amplification matrix of the algorithm (see [12] for details). In Figs. 2 and 3 the high-frequency spectral radii ρ_{∞} of both methods are related to ρ_{∞}^* , which defined as follows:

$$\rho_{\infty}^{*} = \begin{cases} \rho_{\infty}, & \text{for } KR - \alpha \text{ method} \\ (\rho_{\infty})^{2}, & \text{for } KR - \alpha \text{ method} \end{cases}$$
 (17)

Figures 1 and 2 indicate that the PE and the equivalent damping ratio $\overline{\xi}$ for both methods increase with increasing Ω and decreasing values of ρ_{∞}^* For any given Ω the maximum and minimum PE and $\overline{\xi}$ occur for $\rho_{\infty}^*=0$ and 1, respectively. However, in the low-frequency regime, typically defined by $\Omega \leq 0.1\pi$, the PE and $\overline{\xi}$ for both methods are small irrespective of the value of ρ_{∞}^* , which indicates that the low-frequency mode response in an MDOF system is negligibly influenced by the numerical damping. On the other hand, the increase of $\overline{\xi}$ with Ω indicates that any undesired high-frequency mode response can adequately be damped out using the controllable numerical damping.

Both the KR- α and MKR- α Methods are unconditionally stable, second-order accurate. Because the MKR- α method possesses improved overshooting characteristics and optimal numerical dissipation with parameterization with ρ_{∞} it is preferred over the KR- α Method.

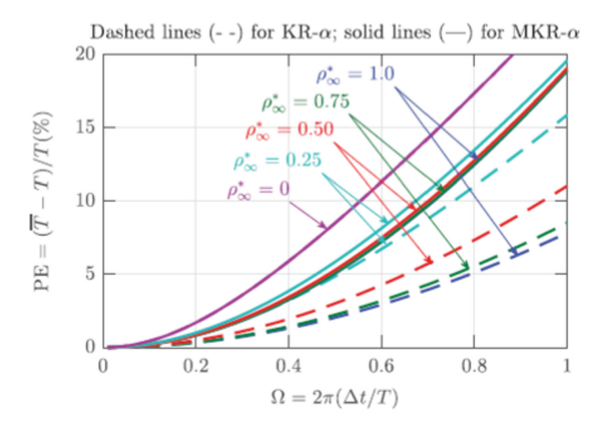


Fig. 2. KR-α and MKR-α Methods: relative period error (PE) as a function of frequency Ω for selected values of ρ_{∞}^* ranging from 0 to 1.0 (from [12]).

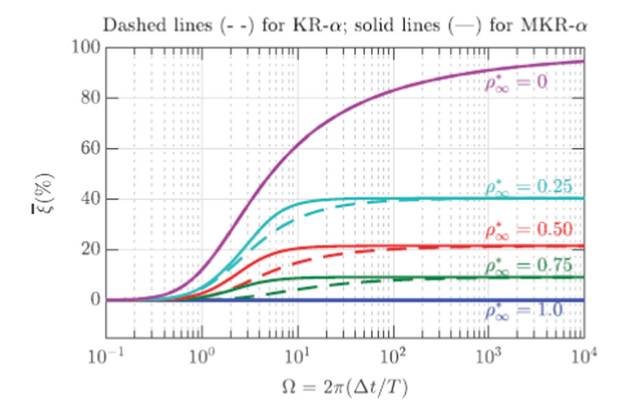


Fig. 3. KR-α and MKR-α methods: equivalent damping ratio $\bar{\xi}$ as a function of frequency Ω for selected values of ρ_{∞}^* ranging from 0 to 1.0 (from [12]).

The procedure for using the MKR- α Method in a RTHS is given below in Table 1. It is also applicable for numerical simulations (i.e., nonlinear dynamic analysis). For choices on the proper selection of ρ_{∞} the reader should consult Eq. (22) in [12].

Table 1. RTHS procedure using the MKR- α method.

1. Initial Calculations

- 1.1 Select time step Δt and high-frequency spectral radii ρ_{∞} .
- 1.2 Determine the equivalent stiffness and damping contributions of the experimental substructure to the structural system's mass M, stiffness K, and damping matrix and C; determine the analytical substructure's contribution to M, K, and C.
- 1.3 Determine the integration parameters α_f , α_m , γ and β using Eqs. (13a), (15), (12a), and (14), respectively; and α_1 , α_2 , and α_3 using Eq. (11).
- 1.4 Form \hat{M}_1 using Eq. (7a) and factorize it.
- 1.5 Form \widehat{M}_2 using Eq. (7b).
- 1.6 Specify X_0 and \dot{X}_0 ; solve Eq. (10) for the initial acceleration \ddot{X}_0 .
- 1.7 Determine $F_{i+1-\alpha_f}$ using Eq. (5d) for all time steps.

2. Calculations for each time step i

- 2.1 Determine $\dot{\mathbf{X}}_{i+1}$ and \mathbf{X}_{i+1} using Eqs. (2) and (3), respectively, and impose them onto the analytical and experimental substructures.
- 2.2 Measure the experimental restoring forces and perform the state determination of the analytical substructure, then calculate $\mathbf{R}_{i+1-\alpha_f}$ using Eq. (9).
- 2.3 Calculate $\dot{X}_{i+1-\alpha_f}$ using Eq. (5b) and determine \ddot{X}_{i+1} using Eq. (6).
- 3. Set i=i+1 and repeat Step 2 for the next time step.

2.2 Explicit-Based State Determination

The integration of the equations of motion requires the determination of the restoring forces. They must be determined in real-time, and hence the state-determination process must be fast and accurate. The discussion of the restoring forces for the experimental substructure is presented later. For the analytical substructure, the determination of the restoring forces \mathbf{R}_{i+1}^a is obtained by subjecting the deformations associated with \mathbf{X}_{i+1} and $\dot{\mathbf{X}}_{i+1}$ to a computational model that represents the analytical substructure. The state determination process must be completed within the time step Δt to avoid accruing a delay, which will lead to a numerical instability. Therefore, the state determination process must be deterministic, and allow only a fixed number of iterations.

Traditional force-based elements [13] are implicit based, where in order to satisfy local equilibrium at the integration points within the element, iteration is used to remove unbalanced internal member forces. Iterating in this manner would jeopardize a RTHS if the elements do not converge within the time step. Kolay and Ricles [14] formulated an explicit force-based beam-column element for conducting RTHS that involve nonlinear analytical substructure response. The element formulation has a fixed number of iterations to satisfy equilibrium, with unbalanced internal member forces and their associated deformations reduced and any residual section forces and deformations are carried over and eliminated in subsequently time steps. A schematic of the element is shown in Fig. 4, where R_{i+1}^a for the element is based on the element nodal forces Q. The nodal forces are in turn based on integrating the element section deformations S(x) along the length of the element. The section deformation S(x) are a function of the element nodal and section deformations, q and d(x), respectively, at each section of the element.

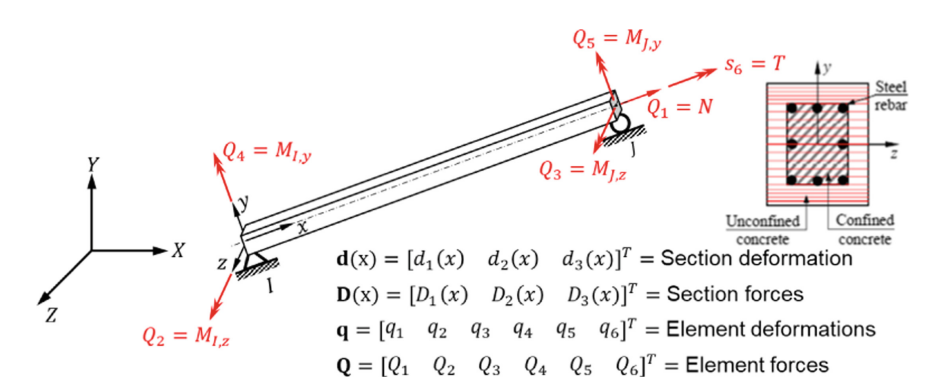


Fig. 4. Forces $[\mathbf{Q}, \mathbf{D}(\mathbf{x})]$ and deformations $[\mathbf{q}, \mathbf{d}(\mathbf{x})]$ at the element and section levels for a three-dimensional frame element in a simply support basic system.

The accuracy of the formulation was assessed by Kolay and Ricles [14] by modelling a highly nonlinear reinforced concrete member in an MRF subject to multidirectional ground motions. The fact that a concrete member was modelled using the formulation lent itself to capturing extensive nonlinear response throughout the element that included reinforcement yielding, concrete cracking, concrete spalling, and concrete crushing. The moment-curvature hysteretic response of a section of one of the beams modelled is shown in Fig. 5 where extensive nonlinear response is evident. The results based on the explicit formulation (identified by CO = Yes) is compared to results obtained using an implicit formulation in the computer program OpenSees [15], in which the average acceleration algorithm of the Newmark method was used [14]. Exceptional agreement between the two is seen in Fig. 5(a), indicating that the residual element deformations are small at the end of the state determination process, and the results therefor accurate. Included in Fig. 5(a) are results based on using the explicit formulation without carrying forward residual unbalanced forces and deformations (identified as CO = No). Divergence from the correct solution is evident. The energy increment EI at the end of the state determination for the same element is shown in Fig. 5(b). The quantity EI represents the energy caused by unbalanced loads and deformations throughout the element. It is desirable to have EI as small as possible, for it is associated with energy that has been injected into the system that should not exist and which will cause the solution to diverge, as shown in Fig. 5(a). The results in Fig. 5(b) show that CO = Yes reduces the EI by five orders of magnitude compared to when CO = No. These results further support the accuracy of the explicit force-based fiber element. A convergence study was performed for a RTHS by Kolay and Ricles [14] where it was found that the state determination for this element formulation can be readily completed within a time step of $\Delta t = 3/1024$ s.

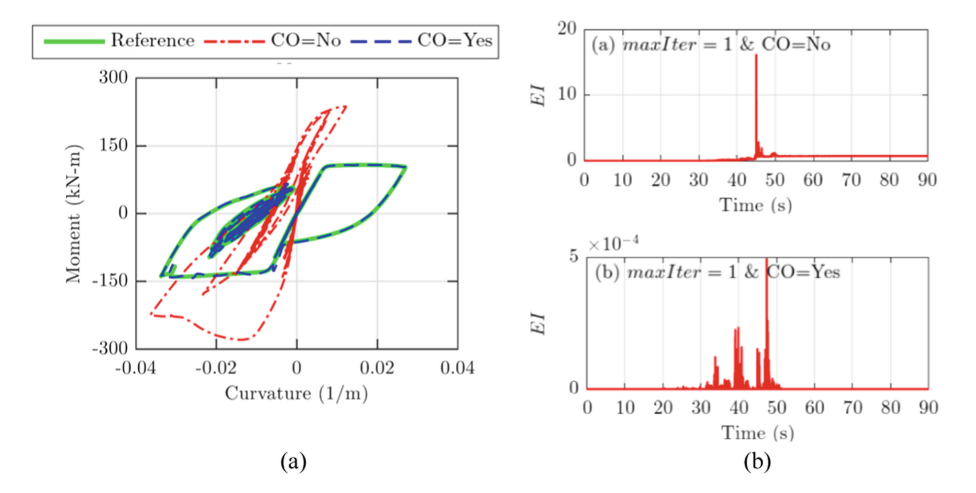


Fig. 5. (a) Section moment-curvature response at south end from numerical simulations of an RC MRF, fixed number of element iterations = 1, with and without carryover (CO); and, (b) associated energy increment (EI) at the end of the element state determination.

2.3 Servo-Hydraulic Actuator Control

The determination of the restoring forces R_{i+1}^e of the experimental substructure of a RTHS are obtained by subjecting targeted deformations x^t to the test setup associated with X_{i+1} and \dot{X}_{i+1} and then measuring the forces required to impose these deformations. These deformations need to be imposed accurately, with minimal amplitude error and delay between the measure deformations x^m and the targeted deformations x^t , otherwise the consequence is the wrong R_{i+1}^e are measured and incorrect RTHS results are obtained. Hydraulic actuators are typically used in a RTHS to impose

displacements to a test structure (also known as the experimental substructure). The inherent nonlinearity of an actuator as well as any nonlinear response of the experimental substructure can result in an amplitude-dependent behavior of the servo-hydraulic system, making it challenging to accurately control the actuator. Accurate actuator control is one of the critical issues to achieve a successful RTHS because it affects the accuracy and stability of the simulation.

An adaptive delay compensation method was developed by the author and his colleagues [16]. The method is based on the time series relationship of the input and output displacements of the combined servo-hydraulic and experimental substructure systems. The method is referred to as the adaptive time series (ATS) compensator. The ATS compensator updates the coefficients of the system at each time step of the RTHS using regression analysis. The system identification procedure does not involve a user-defined adaptive gain, which is one of the advantages of the ATS compensator over other adaptive compensation methods.

In a RTHS the integration algorithm computes the structural displacement response for each time step. The computed displacement is imposed onto the analytical and experimental substructures in real-time, where for the experimental substructure the actuator target displacement x^t is obtained by considering the relationship between the structural DOF and actuator DOF. The dynamics of servo-hydraulic system combined with the experimental substructure inevitably causes a time delay and amplitude change in the actuator output displacement.

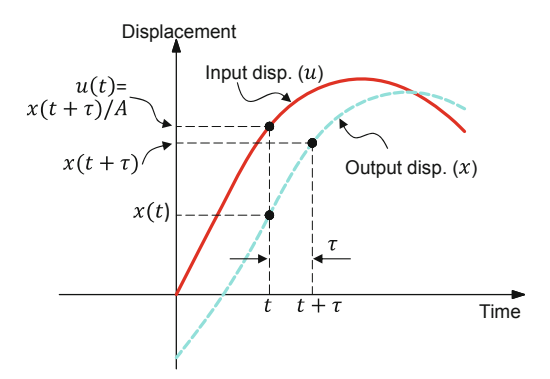


Fig. 6. Input and output displacement relationship of servo-hydraulic system with experimental substructure

If the output displacement of the servo-hydraulic system with experimental substructure, x, has a constant time delay of τ and an amplitude error A (where A is the amplitude error factor that represents the ratio between the output and input displacement amplitudes) with respect to the input displacement to the actuator, u, then u at time t can be expressed as follows:

$$u(t) = \frac{1}{A}x(t+\tau) \tag{18}$$

Figure 6 shows the relationship between x and u. If x is n-time differentiable in the neighborhood of t, Eq. (18) can be approximated using a Taylor series

$$u(t) \cong \frac{1}{A} \left[x(t) + \tau \dot{x}(t) + \frac{\tau^2}{2} \ddot{x}(t) + \dots + \frac{\tau^n}{n!} \frac{d^n x}{dt^n} \right]$$
 (19)

Thus, the input displacement of the actuator at time t can be expressed by the power series of the time delay and the output response at time t. If the higher order terms beyond the 2^{nd} order term are ignored in Eq. (19), this equation becomes similar to the actuator delay compensation procedure based on the constant acceleration method [17–19] when there is no amplitude error (i.e., A = 1.0).

To obtain accurate experimental results in a RTHS, the time delay and amplitude error need to be appropriately compensated whereby the target displacement x^t is achieved by the actuator (i.e., the measured actuator displacement x^m is equal to x^t). The procedure to minimize actuator delay presented in this paper is shown conceptually in Fig. 7, where a compensated displacement command u^c is sent to the actuator to attempt to have x^m match x^t . u^c is obtained by considering the compensated displacement command as the actuator input displacement u in Eq. (19) and substituting x^m for x. The final result for u^c is then obtained by substituting x^t for x^m , and expressed in the discrete time domain as:

$$u_k^c = a_0 x_k^t + a_1 \dot{x}_k^t + \dots + a_n \frac{d^n x_k^t}{dt^n}$$
 (20a)

where

$$a_j = \frac{\tau^j}{Aj!}, \quad j = 0, 1, \dots, n$$
 (20b)

In Eq. (20a) the subscript k is a time index (e.g., $u_k^c = u^c(t_k)$, where time $t_k = k\Delta t$ and Δt is the time step size of the discrete time domain). Equation (20a) is similar to that used in the model-based feedforward compensator by Phillips and Spencer [20], who based their compensator on a 3rd order inverse transfer function of the linearized servohydraulic actuator system.

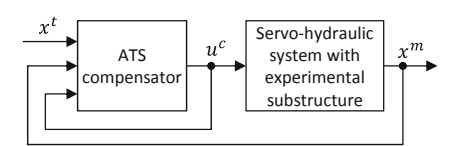


Fig. 7. Schematic of actuator delay compensation with feedback (ATS compensator); (x^t) : actuator target displacement, u^c : compensated actuator input displacement command, x^m : measured actuator displacement).

In general, the combined servo-hydraulic actuator system and experimental substructure can exhibit nonlinear behavior due to the complexity of the servo-valve dynamics as well as any nonlinearity in the experimental substructure, resulting in a variable time delay and amplitude error. When nonlinearities are predominant, Eq. (20a), which is for a system that has a constant time delay and amplitude error, will result in an inaccurate compensated input displacement command to the actuator. In order to account for this nonlinearity, it is suggested to vary a_j adaptively in accordance with the response of the actuator. This compensation method in the equally spaced discrete time domain is referred to in herein as the adaptive time series (ATS) compensator.

In the ATS compensator, the coefficients a_j at time t_k are identified from the relationship between the input and measured actuator displacements over the previous $q\Delta t$ time duration (i.e., from time t_{k-q} to t_{k-1}). The least squares method is used to obtain values for the coefficients a_j , where the objective function to be minimized, J_k , is defined as

$$J_k = \sum_{i=1}^{q} \left(u_{k-i}^c - u_{k-i}^{est} \right)^2 \tag{21}$$

In Eq. (21) u_{k-i}^c is the compensated input actuator displacement at time t_{k-i} , and u_{k-i}^{est} is the estimated compensated input actuator displacement at time t_{k-i} based on Eq. (20a) using the measured actuator displacement x_{k-i}^m at time t_{k-i} and its time derivatives:

$$u_{k-i}^{est} = a_{0k} x_{k-i}^m + a_{1k} \dot{x}_{k-i}^m + \dots + a_{nk} \frac{d^n x_{k-i}^m}{dt^n}$$
 (22)

The values of the coefficients a_{jk} $(j = 1, 2, \dots, n)$ in Eq. (22) are identified using the measured actuator motions over the previous $q\Delta t$ time duration and the standard least squares procedure, as noted above, where it can be shown that:

$$\mathbf{A} = \left(\mathbf{X}_{m}^{T} \mathbf{X}_{m}\right)^{-1} \mathbf{X}_{m}^{T} \mathbf{U}_{\mathbf{c}} \tag{23}$$

where, $\mathbf{A} = [a_{0k}a_{1k}\cdots a_{nk}]^T$, $\mathbf{X}_m = [\mathbf{x}^m\dot{\mathbf{x}}^m\cdots \frac{d^m}{dt^n}(\mathbf{x}^m)]$, $\mathbf{x}^m = [x_{k-1}^mx_{k-2}^m\cdots x_{k-q}^m]^T$, and $\mathbf{U}_{\mathbf{c}} = [u_{k-1}^cu_{k-2}^c\cdots u_{k-q}^c]^T$. With the values for the coefficients a_{jk} identified, the compensated input actuator displacement at time t_k is calculated using Eq. (20a):

$$u_k^c = a_{0k}x_k^t + a_{1k}\dot{x}_k^t + \dots + a_{nk}\frac{d^n x_k^t}{dt^n}$$
 (24)

Comparing the 1st and 2nd coefficients in Eqs. (20a) and (24), the two coefficients in the latter can be related to the amplitude error factor and time delay using Eq. (20b), where:

$$A_k \cong \frac{1}{a_{0k}}, \quad \tau_k \cong \frac{a_{1k}}{a_{0k}} \tag{25a,b}$$

When the amplitude error is not significant, i.e., $A_k \cong 1$, a_{1k} is approximately equal to τ_k .

Good actuator displacement tracking can be achieved with the use of higher order terms in Eq. (24) for a pre-defined displacement input with its pre-defined time derivatives. In a real-time hybrid simulation, however, the use of a higher order term may not be always desirable since the accuracy of the higher order time derivatives of the target displacement x^t can be significantly affected by the noise inherent in the experimental restoring force R_{i+1}^e that introduces noise into x^t through the integration algorithm. In addition, the effect of a higher order term on the compensated displacement would be negligible when the time delay is small as can be seen in the coefficients of Eq. (20a). For this reason, a 2^{nd} order system (n=2) is presented herein for the calculation of the compensated input actuator displacement, whereby:

$$u_k^c = a_{0k} x_k^t + a_{1k} \dot{x}_k^t + a_{2k} \ddot{x}_k^t \tag{26}$$

The target velocity and acceleration are estimated by using the finite difference method, where

$$\dot{x}_{k}^{t} = \frac{x_{k}^{t} - x_{k-1}^{t}}{\Lambda t}, \quad \ddot{x}_{k}^{t} = \frac{x_{k}^{t} - 2x_{k-1}^{t} + x_{k-2}^{t}}{\Lambda t^{2}}$$
(27)

The same method can be applied to the measured actuator displacement to obtain the actuator velocity \dot{x}^m and acceleration \ddot{x}^m that are used in Eq. (22). However, unlike the target displacement, the measured actuator displacement inevitably contains sensor noise which can subsequently result in a large error in the estimation of \dot{x}^m and \ddot{x}^m when the finite difference method is used. A low pass filter is therefore used to remove high frequency noise from x^m so that a better estimate of \dot{x}^m and \ddot{x}^m is achieved using the finite difference method. Since the use of a filter introduces a time delay, the same low pass filter is applied to the compensated actuator input displacement u^c_{k-i} in Eq. (21) to obtain a synchronized set of data for u^c_{k-i} and u^{est}_{k-i} . That is, the coefficients of Eq. (24) at time t_k are determined based on the previous data between time $t_{k-q} - \phi$ and $t_{k-1} - \phi$, where ϕ is the time delay introduced by the low pass filter.

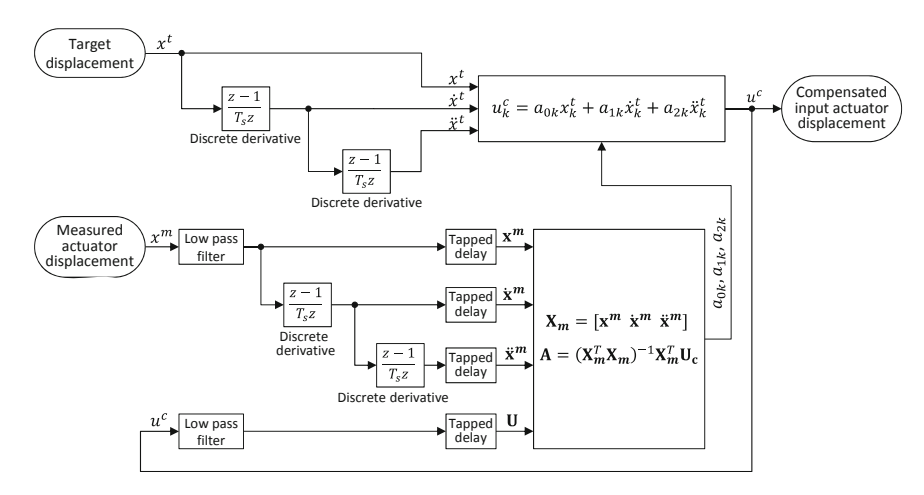


Fig. 8. Simulink block diagram for ATS compensator.

The RTHS performed at the Lehigh NHERI Experimental Facility uses a real-time integrated control IT architecture, where workstations with real-time operating systems are connected with shared memory [21]. Figure 8 shows a block diagram [16] associated with the implementation of the ATS compensator using Simulink [22]. The Simulink block diagram is compiled into real-time executable code, enabling it to be ingested into the Lehigh NHERI Experimental Facility's real-time integrated control IT architecture [21]. The tapped delay in the Simulink block diagram enables the values in x^m and u^c to be extracted for use in Eq. (23).

The ATS has been experimentally validated [Chae et al.] and used to performed numerous successful RTHS [10, 14, 23–30].

3 Applications of Hybrid Simulation Towards Improving the Seismic Resiliency of Structural Steel Buildings

RTHS has been used by the author and his colleagues to develop and validate several concepts to improve the seismic resiliency of structural steel lateral force resisting systems (LFRS) for buildings. Examples of some of these concepts are given in this section of the paper include: self-centering moment resisting frame systems, braced frame systems with nonlinear viscous dampers, and a tall building with a nonlinear viscous damped outrigger system.

3.1 Self-centering Moment Resisting Frame Systems

Ricles et al. [31–34] developed the self-centering moment resisting frame (SC-MRF) concept for promoting the seismic resiliency of steel moment resisting frame systems. An SC-MRF is characterized by connection gap opening and closing at beam-column interfaces under earthquake loading. The SC-MRF uses high strength post-tensioning (PT) strands to precompress the beams to the columns, as shown in Fig. 9(a) and (b), and to close the gaps that develop under earthquake loading, returning the frame to its initial position (i.e., the frame is "self-centering"), Fig. 9(d). In Fig. 9(d), θ_r is the relative rotation at the interface between the column and beam. It is zero prior to gap opening. In their study [35, 36], Lin et al. had a beam web friction device included in each beam-column connection to dissipate energy under seismic loading (see Fig. 9(c) and (e)). Unlike a special steel moment-resisting frame with welded connections (W-SMRF), it had been hypothesized by the researchers [32–34] that an SC-MRF can be designed to survive the design basis earthquake (DBE) without structural damage, leading to the potential for immediate occupancy (IO) performance, and to suffer only modest damage under the maximum considered earthquake, leading to collapse prevention performance. Lin et al. [35, 36] therefore performed large-scale testing of buildings with SC-MRFs to validate this hypothesis.

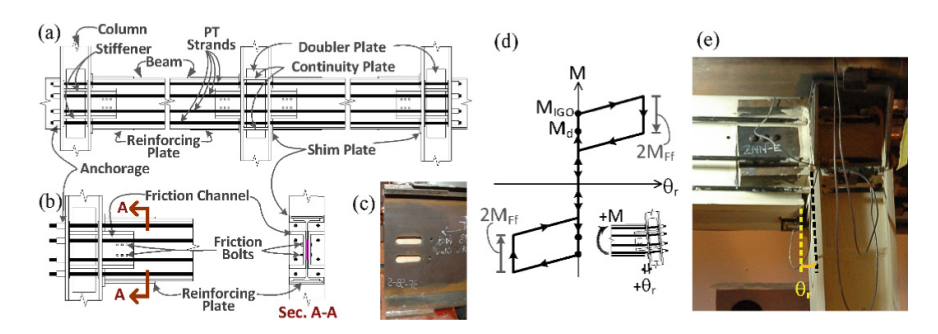


Fig. 9. (a) Schematic of elevation of a 2-bay SC-MRF with PT strands and WFDs, (b) connection details, (c) slotted holes in the beam web, (d) conceptual M- θ_r behavior and (e) gap opening, (from Lin et al. [35]).

Hybrid Simulation Configuration. In the study by Lin et al. [35, 36], a 7-bay, 4-story SC-MRF prototype building was designed for a location in the Los Angeles area using a design procedure described in Lin et al. [35] and Garlock et al. [37]. The fundamental period of the building in the plane of the SC-MRFs was 1.51 s. A 0.6-scale model of two bays of the SC-MRF building was constructed in the laboratory (see Fig. 10) and subjected to simulated earthquakes using the hybrid simulation method to validate the performance of the design and its resiliency under severe earthquake ground motions. In the hybrid simulations the SC-MRF was physically modelled (i.e., was the experimental substructure) with the remaining part of the structure consisting of the gravity load system and its P- Δ effects modelled as part of the analytical substructure. The test structure (i.e., the experimental substructure) included the floor diaphragm and lateral force collector system (see Fig. 10(a, c)). The diaphragm is attached to only one bay of the SC-MRF to avoid restraining connection gap opening in the test frame (see Figs. 10 (a, c) and 11). Hybrid simulations were performed using an ensemble of ground motions, with records scaled to the design basis earthquake (DBE) level (see Table 2) and the maximum considered earthquake (MCE) level (see Table 3). The DBE and MCE ground motions have a 474 and 2,475-year return period, respectively. The time step Δt used in the hybrid simulations was 16/1024 s (i.e., 0.0156 s). The value for Δt was arrived at by a convergence study to assure the accuracy of the results. A value of $\rho_{\infty} = 1.0$ was used, with an expanded time scale of 100 (i.e., the simulations were not done in real-time).

Hybrid Simulation Results. The DBE RTHS results showed that the SC-MRF demonstrated damage-free behaviour. There was minimal residual drift under the DBE, as evident in the results tabulated in Table 4 for residual story drift after each simulation. Figure 12 shows the floor horizontal displacement time history for four different ground motions scaled to the DBE, where no permanent lateral displacement is evident at the end of each test. Gap opening occurred at the beam-column interface of the connection (see Fig. 13). Under the MCE level, the residual drift remained small (see Table 5 and Fig. 14). As in the DBE, the SC connections showed gap opening with self-centering under the MCE (see Fig. 15). There was beam flange yielding but no

yielding in the beam web or PT strands. The occurrence of these last two limit states would lead to a loss of PT force and moment capacity of the beam-to-column SC connection. No signs of collapse under the MCE were evident. The SC-MRF essentially performed at the IO level under the MCE.

The hybrid simulation methods enabled realistic studies to be performed to assess the seismic performance of an SC-MRF that is the LFRS of a building. The structural damage-free performance of the SC-MRF test-frame during the DBE and MCE hybrid simulations demonstrates the potential for IO performance of SC-MRF buildings at the DBE seismic input level. The hybrid simulations also demonstrated that the floor diaphragm forces affect the post gap opening stiffness of the SC-MRF connection M- θ_r response [35, 36]. This effect must be included in design, as shown by Garlock et al. [37]. A comparable SMRF was designed and analysed under the DBE and MCE [38]. It was found that the conventional SMRF suffers significant damage in the form of yielding in the beams compared to the building with SC-MRFs, leading to residual drift of the structure. Hence, the seismic performance of the SC-MRF is superior compared to that of a conventional SMRF.

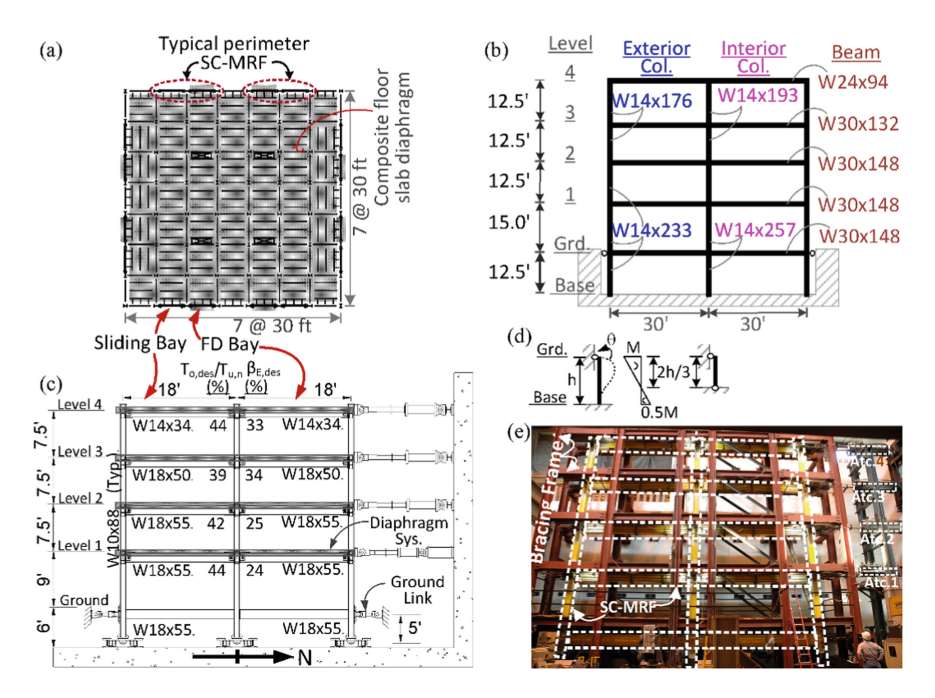


Fig. 10. (a) Prototype building plan, (b) prototype SC-MRF elevation, (c) SC-MRF test frame elevation, (d) basis for adjusted basement story height and (e) SC-MRF test frame in laboratory, (from Lin et al. [35]).

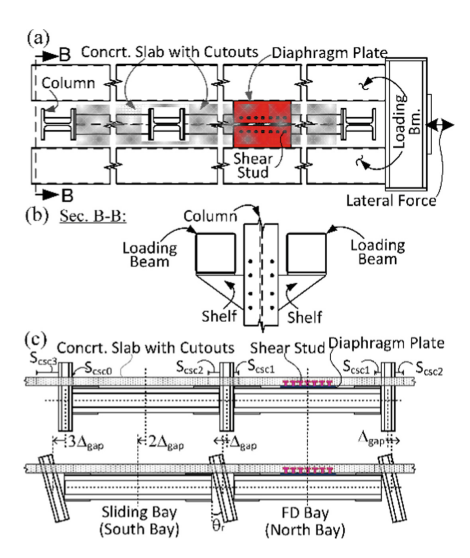


Fig. 11. Schematic of (a) floor diaphragm system, (b) shelves on the column, and (c) gap opening without floor diaphragm restraint, [from Lin et al. [35]).

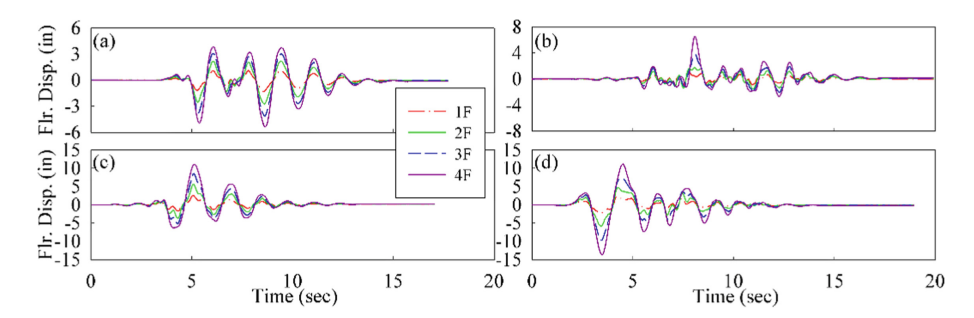


Fig. 12. Floor displacements time histories from (a) DBE-1 (b) DBE-2, (c) DBE-3, and (d) DBE-4, (from Lin et al. [35]).

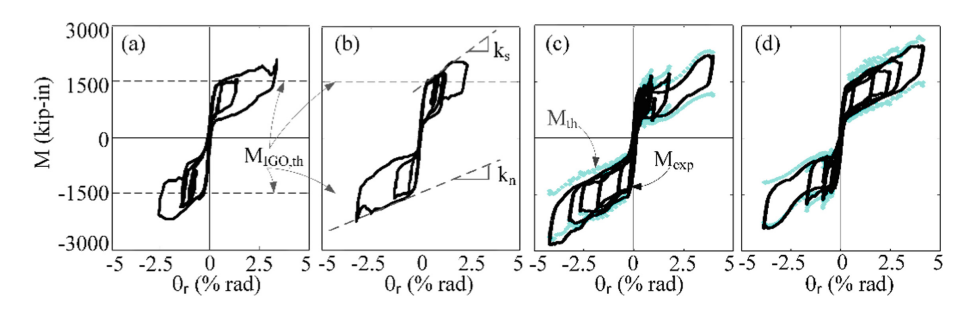


Fig. 13. Typical M- θ_r responses, (a) 3FSS and (b) 3FSN connections from DBE-3, and (c) 3FSS and (d) 3FSN connections from DBE-4, (from Lin et al. [35]).

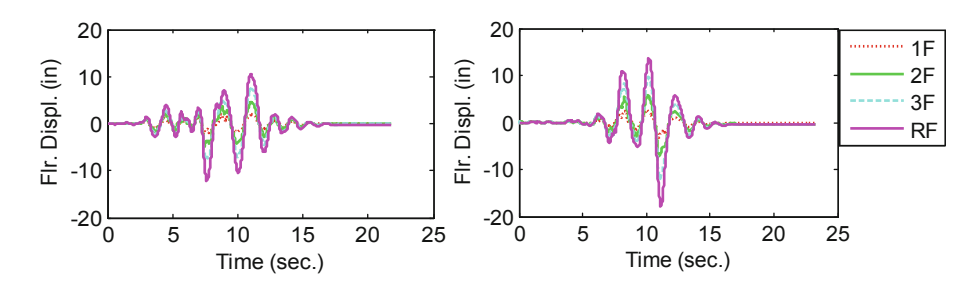


Fig. 14. Floor displacements time histories from (a) MCE-1 and (b) MCE-2, (from Lin et al. [36]).

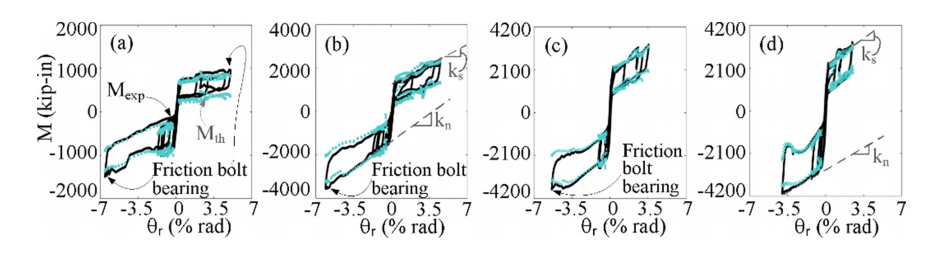


Fig. 15. M- θ_r responses of SS connection from MCE-2: (a) 4th, (b) 3rd, (c) 2nd, and (d) 1st floors, (from Lin et al. [36]).

Table 2. Hybrid simulation matrix for DBE performance evaluations.

Test	Event	Record	Scale factor
DBE-1	1979 Imperial Valley	H-ECC002	0.94
DBE-2	1989 Loma Prieta	SJTE315	2.23
DBE-3	1994 Northridge	LOS000	1.18
DBE-4		CNP196	1.28

Table 3. Hybrid simulation matrix for MCE performance evaluations.

Test	Event	Record	Scale factor
MCE-1	1979 Imperial Valley	5082-235	2.74
MCE-2	1989 Loma Prieta	STM090	2.08

Test	Residual story drift (%rad)									
	1st story 2nd story 3rd story 4th story									
DBE-1	-0.007	-0.028	-0.040	-0.047						
DBE-2	0.014	0.035	0.061	0.045						
DBE-3	0.074	0.063	0.023	0.008						
DBE-4	-0.028	-0.068	-0.075	-0.057						

Table 4. Residual story drift after DBE simulations.

Table 5. Residual story drift after MCE simulations.

Test	Residual story drift (%rad)								
	1st story	2nd story	3rd story	4th story					
MCE-1	-0.031	-0.031	-0.056	-0.094					
MCE-2	-0.180	-0.110	-0.086	-0.059					

3.2 Braced Frame Systems with Nonlinear Viscous Dampers

Passive damping devices have become established as a means to improve the seismic performance of building structures (e.g., [39, 40]). Current seismic design provisions, such as those in ASCE/SEI 41-06 [41], FEMA P-750 [42], and ASCE/SEI 7-16 [43], include provisions for passive damping devices. Passive damping devices include nonlinear viscous dampers. These types of dampers are appealing because the force output from a damper is capped, i.e., the damper force output does not continue to increase with velocity. By controlling the maximum damper force, members in a system (e.g., adjacent diagonal bracing, beams, columns) can be protected from being overloaded. The seismic response of structures with nonlinear viscous dampers has been studied by numerous researchers, including Pekcan et al. [44], Terenzi [45], Lin and Chopra [46], and Sorace and Terenzi [47]. Most of this previous work was analytical or numerical; there have been few experimental investigations of the large-scale system-level behavior of structures with nonlinear viscous dampers.

Dong et al. [24] therefore performed an experimental study of the seismic performance of a large-scale multistory steel frame building structure with nonlinear viscous dampers. The purpose was to investigate the behavior of building systems with nonlinear viscous dampers subjected to strong ground motions. Items of interests included the interaction of the dampers with the lateral load resisting system, the effectiveness of the dampers in reducing seismic damage, and whether the design base shear of the system can be reduced when dampers are used to control drift. To perform the experiment it was necessary to conduct RTHS involving the complete building system, for the dampers are load rate dependent.

Real-Time Hybrid Simulation Configuration. The prototype structure is shown in Fig. 16 and is a three-story office building assumed to be located on a stiff soil site in Pomona, California. The layout of the building is symmetric in plan as shown in Fig. 16(a). The prototype structure was designed according to provisions of ASCE7-10

[48], and criteria from American Institute of Steel Construction (AISC) [49–51]. Wide flange ASTM standard A992 steel sections were selected for the beams and columns. Moment resisting frames (MRFs) and damper braced frames (DBFs), the latter having nonlinear viscous dampers placed at each floor served as the LFRS for the structure. The nonlinear viscous dampers had a force capacity of 600 kN and stroke of ±125 mm in the scaled DBF, with one damper in each story. Considering the laboratory limitations, the prototype structure was scaled by a factor of 0.6 to develop the test structure, shown in Fig. 17. Due to the symmetry of the floor plan as noted previously, the test structure consists of one MRF, an associated DBF, and the gravity load system and seismic mass tributary to the MRF and DBF. In the test structure, only 2/3 of the true height of basement column is included in the structure, and the column is pinned at an assumed inflection point at 1/3 of the true column height from the bottom of the basement.

The ATS compensator was used for the RTHS. The root mean square (RMS) over a one second window of the actuator command was used to activate and deactivate the ATS coefficient updating. When the RMS value was about 1 mm the ATS was triggered, and turned off when below the RMS value.

The characteristics of the dampers is shown in Fig. 18, where the results from characterization tests on a typical damper are shown. The load-rate dependency is apparent from the results of the characterization tests.

A test structure with a full base shear strength MRF design (i.e., D100V) and test structures with reduced (75 and 60%) base shear strength MRF designs (i.e., D75V and D60V) were studied. Earthquake simulations using ensembles of DBE and MCE level ground motions were conducted using real-time hybrid simulation (RTHS). For the RTHS, the MRF and the gravity load system were modelled numerically as the analytical substructure, while the DBF was tested in the laboratory as the experimental substructure. The RTHS used a time step of $\Delta t = 3/1024$ s, with $\rho_{\infty} = 0.866$.

Ground motions that represent the design basis earthquake (DBE) and maximum considered earthquake (MCE) were used as input for the RTHS. An ensemble of 14 ground motions was selected for the DBE level RTHS. For the MCE level RTHS, an ensemble of 12 ground motions was selected for the D100V and D75V structures, and another ensemble of 7 ground motions was selected for the D60V structure. The Pomona site was selected because the uniform hazard spectra (UHS) with a 10% (DBE) and 2% (MCE) probability of exceedance (POE) in 50 years, respectively, are consistent with the ASCE 7-10 DBE and MCE spectra. Each ground motion record was scaled so that the median spectral acceleration for the ensemble matched the target UHS over a period range of 0.2–4.0 s. Details of the process for selecting and scaling of the ground motions are given by Dong et al. [24].

A photograph of the experimental substructure, consisting of the DBF, is shown in Fig. 19. The DBF test structure was not expected to develop damage. Damage, if any, was expected to develop only in the analytically modelled MRF. The RTHS involved using the same analytical substructure throughout the test program (with the mass scaled to achieve the prescribed design base shear). For each subsequent RTHS the state of the analytical model was readily reset to its virgin state and the analytical and experimental substructures conveniently reused throughout the test program. Complete details about the test program can be found in Dong et al. [23–25].

Real-Time Hybrid Simulation Results. The story drift ratio time histories from the DBE level RTHS using the HECTOR-11625090 record for the D100V, D75V, and D60V structures are shown in Fig. 20. Negligible residual story drifts are seen at the end of the simulations, indicating that even the test structures with reduced strength designs exhibited a nearly elastic response under the DBE. Figure 21 shows the story drift ratio time histories from the MCE level RTHS using the 1999 Chi-Chi earthquake TCU055-N record. The story drift ratio time histories for the D100V and D75V structures are almost zero at the end of the simulations, but residual story drifts are seen at the end of the simulation for the D60V structure. The second story has a larger drift ratio than the first and third stories for each structure. The mean and coefficient of variation (COV) of the peak story drift ratios for the ground motion ensembles from the RTHS are summarized in Table 6. The second story peak story drift ratio is larger than the first and third stories for all the structures, and the peak story drift increases as the base shear design strength decreases under both the DBE and MCE ground motions. The COV for the peak story drift ratio is less than 0.25, which suggests relatively modest dispersion of the peak story drift ratios.

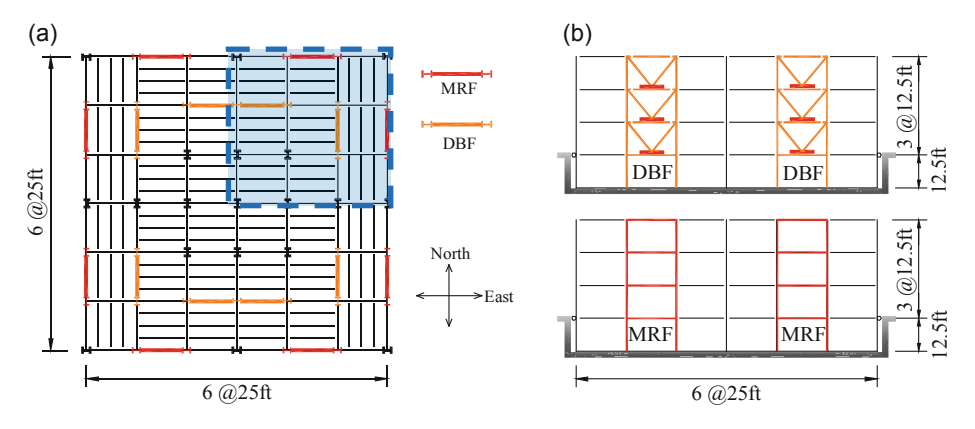


Fig. 16. Prototype building (1 ft. = 0.3048 m): (a) plan view; (b) section view (from Dong et al. [24])

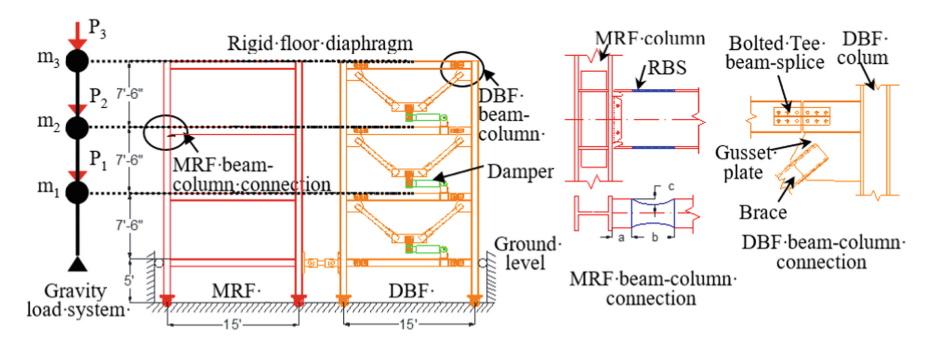


Fig. 17. Test structure (1 ft. = 0.3048 m) (from Dong et al. [24]).

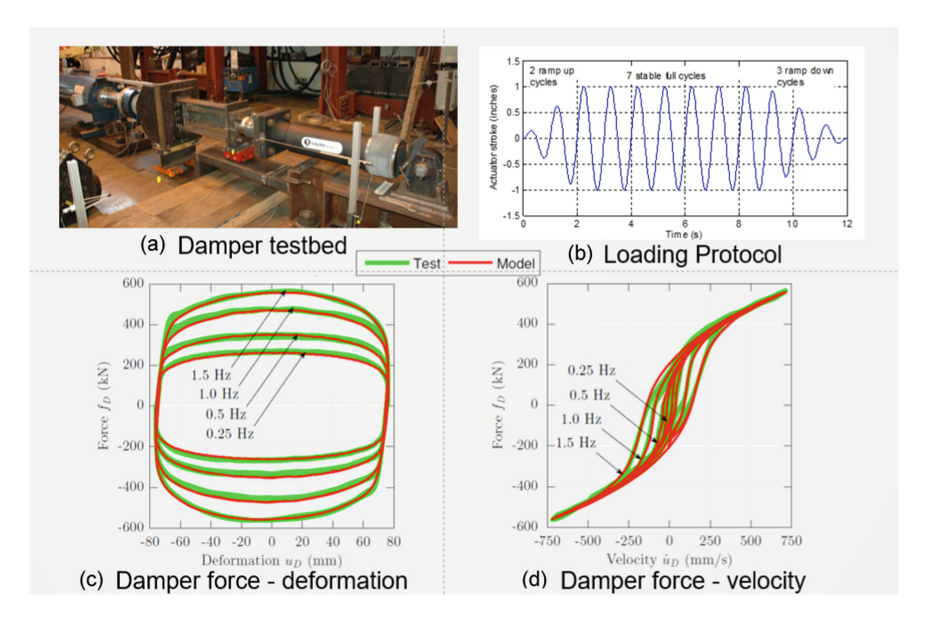


Fig. 18. Damper characterization testing of nonlinear viscous dampers: (a) testbed; (b) loading protocol; (c) damper force-deformation; and, (d) damper force-velocity relationship.



Fig. 19. Photograph of the experimental substructure (from Dong et al. [24]).

The mean of the residual story drifts from the ensemble of ground motions for each hazard level are given in Table 7. Under the DBE ground motions, the mean residual story drift ratios are quite small (negligible). Under the MCE ground motions, the mean residual story drift ratios for the D100V structure are also quite small (0.1% or less), indicating that the D100V structure has very little inelastic response that results in permanent deformation. The MCE mean residual story drift ratios for the D75V and D60V structures are less than 0.2%. The relatively large COVs for the residual story drift ratios suggest that the characteristics of the individual ground motions in the ensembles

(the so-called record-to-record variability) strongly affect the residual story drift ratio. The residual story drift ratios for all structures for all MCE level ground motions are less than 0.5% rad, which is considered to be the level of residual story drift that impairs operation of moveable components of a building such as doors, windows, and sliding partitions according to Galambos and Ellingwood [52], Ellingwood [53], and McCormick et al. [54]. These results suggest a high probability of good functional performance of the prototype buildings with dampers after an MCE level ground motion.

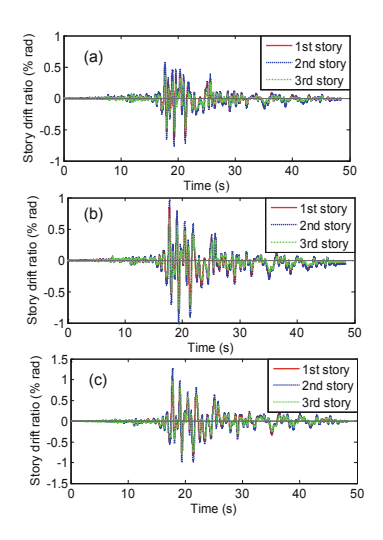


Fig. 20. Story drift ratio time histories from DBE level RTHS using HECTOR-11625090 record: (a) D100V; (b) D75V; and (c) D60V. (from Dong et al. [24]).

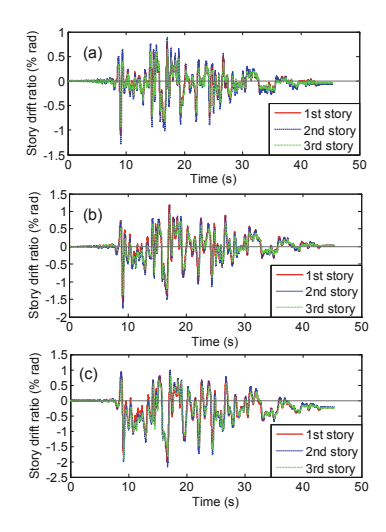


Fig. 21. Story drift ratio time histories from MCE level RTHS using TCU055-N record: (a) D100V; (b) D75V; and (c) D60V. (from Dong et al. [24]).

Structure	DBE						MCE					
	Mean (% rad)		COV			Mean (% rad)			COV			
	1st	2nd	3rd	1st	2nd	3rd	1st	2nd	3rd	1st	2nd	3rd
	story	story	story	story	story	story	story	story	story	story	story	story
D100V	0.69	0.76	0.53	0.18	0.17	0.13	1.20	1.38	1.00	0.22	0.22	0.21
D75V	0.85	0.98	0.74	0.17	0.16	0.15	1.53	1.86	1.52	0.21	0.19	0.21
D60V	1.00	1.17	0.95	0.16	0.17	0.15	1.88	2.21	1.88	0.14	0.12	0.12

Table 6. Peak story drift ratios.

Table 7. Residual story drift ratios.

Structure	DBE						MCE					
	Mean (% rad)			COV			Mean (% rad)			COV		
	1st	2nd	3rd	1st	2nd	3rd	1st	2nd	3rd	1st	2nd	3rd
	story	story	story	story	story	story	story	story	story	story	story	story
D100V	0.02	0.03	0.01	1.00	0.98	0.83	0.06	0.06	0.06	0.59	0.59	0.59
D75V	0.04	0.05	0.03	0.47	0.51	1.02	0.13	0.17	0.15	0.92	0.81	0.83
D60V	0.05	0.06	0.05	1.01	1.09	0.95	0.20	0.20	0.20	0.56	0.83	0.72

The time histories of the targeted x_n^t and measured x_n^m actuator displacements from the RTHS for the DBE and MCE level ground motions are given in Fig. 22. It can be seen in Fig. 22(a) that the structure has a DBE maximum floor displacement of 18, 36, and 48 mm for the $1^{\rm st}$, $2^{\rm nd}$, and 3rd floor, respectively. The normalized RMS error between x_n^t and x_n^m is 3.8%, 2.4%, and 2.3% for the $1^{\rm st}$, $2^{\rm nd}$, and $3^{\rm rd}$ floor, respectively. Under the MCE, the maximum floor displacement in Fig. 22(b) is 31, 64, and 86 mm for the 1st, 2nd, and 3rd floor, respectively. The normalized RMS error between x_n^t and x_n^m is 3.8%, 1.8%, and 1.9% for the $1^{\rm st}$, $2^{\rm nd}$, and $3^{\rm rd}$ floor, respectively. The results shown in Fig. 22 were typical, where good agreement between x_n^t and x_n^m is observed in all of the DBE and MCE RTHS.

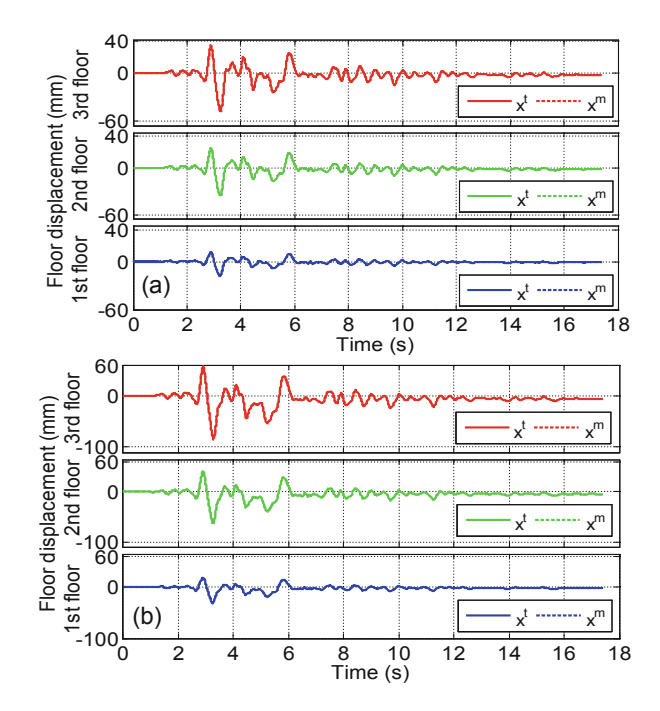


Fig. 22. Floor displacement response from (a) DBE and (b) MCE level RTHS; Rinaldi Receiving Station 1994 Northridge Earthquake (after Dong et al. [23]).

Figure 23 shows the variation of the compensator coefficients for the ATS compensator during this MCE level RTHS. It is observed that except for the rapid change at the time of 2.0 s when structural response starts to increase, the coefficients were fairly constant during the RTHS. The coefficient a_0 of each floor varies within the range of 1.0 to 1.1, and has values relatively close to 1.0 over the time period of 2.0 s to 6.0 s when structural response is significant (see Fig. 22). This indicates the required compensation for amplitude error, A_k (see Eq. (25a) is relatively small when the structural response is large. The coefficient a_1 of each floor varies within a range up to 20% of the initial value and indicates the compensation for time delay, τ_k (see Eq. (25b)) is approximately 0.05, 0.035, and 0.02 s for the $1^{\rm st}$, $2^{\rm nd}$, and $3^{\rm rd}$ floor displacement response, respectively. This amount is considered to be a significant correction compared to the time step of $\Delta t = 3/1024$ s used in the simulation. The ATS compensator enabled these exceptional results to be achieved in all of the RTHS.

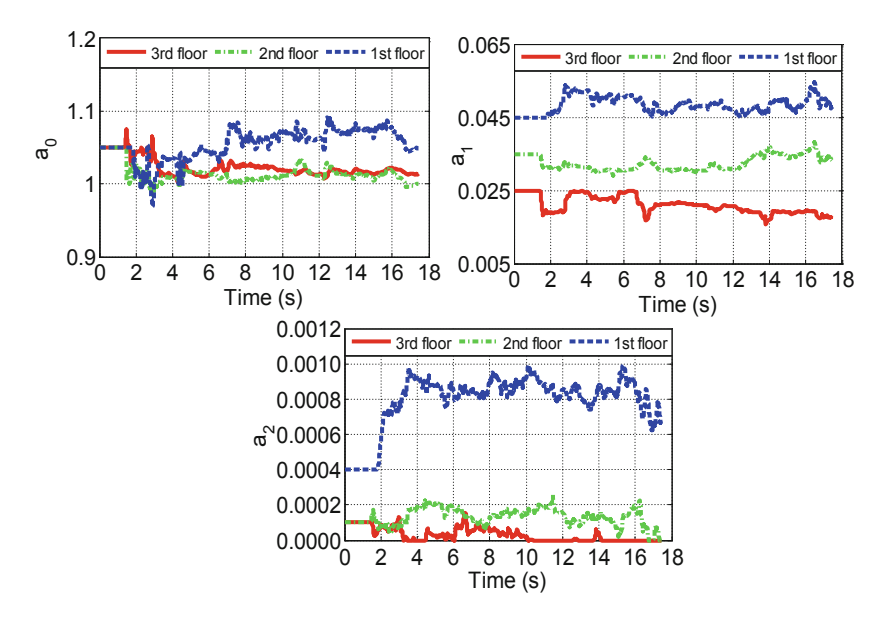


Fig. 23. Variation of compensator coefficients over time history of MCE level RTHS (after Dong et al. [23]).

Table 8 presents the mean and COV of the peak total floor accelerations from the RTHS. The maximum mean peak total floor accelerations of the D75V and D60V structures are 14 and 25% less than that of the D100V structure under the DBE, and 9 and 25% smaller than that of the D100V structure under the MCE, respectively. These results show that reduced base shear design strength structures (D75V and D60V) have smaller total floor acceleration response than a full-strength structure (D100V). This suggests that damage to acceleration-sensitive nonstructural components can be reduced by reducing the base shear design strength for the structure.

Structure	DBE					MCE						
	Mean (g)		COV			Mean (g)			COV			
	1st	2nd	3rd	1st	2nd	3rd	1st	2nd	3rd	1st	2nd	3rd
	floor	floor	floor	floor	floor	floor	floor	floor	floor	floor	floor	floor
D100V	0.38	0.43	0.56	0.20	0.13	0.09	0.51	0.58	0.68	0.12	0.11	0.08
D75V	0.34	0.39	0.48	0.19	0.14	0.12	0.50	0.52	0.62	0.15	0.13	0.08
D60V	0.31	0.35	0.42	0.19	0.15	0.14	0.50	0.47	0.51	0.16	0.12	0.06

Table 8. Peak total floor acceleration.

The effects of elastic flexibility in the damper force path of the test structures (i.e., including the connections, braces, beams, and columns of the DBF), designed and constructed under practical conditions, were observed in the RTHS results as shown in Fig. 24. The figure shows that the story drifts are larger than the damper deformations and the damper force-story drift hysteresis loops are inclined relative to the damper force-damper deformation hysteresis loops. This elastic flexibility is within the force path from the dampers to the seismic mass degrees of freedom (DOF), including the connections, braces, beams, and columns of the DBF. This elastic flexibility causes the viscous damper forces to be partially in phase with the story drifts (i.e., when the story drifts are at their peak values, the damper forces are large). This in-phase behavior of the damper forces with story drifts results in a combined axial force and bending moment response in the DBF columns with large axial forces at the times of peak bending moments (see Fig. 25). Such combinations of axial forces and bending moments should be considered in the design of the columns of frames with nonlinear viscous dampers. This in-phase damper force behavior also results in significant contributions of damper forces to the total story shear forces of the test structure at the times of peak story drifts, and as a result, this in-phase damper force behavior stiffened the test structures and reduced the story drift response (see Fig. 26).

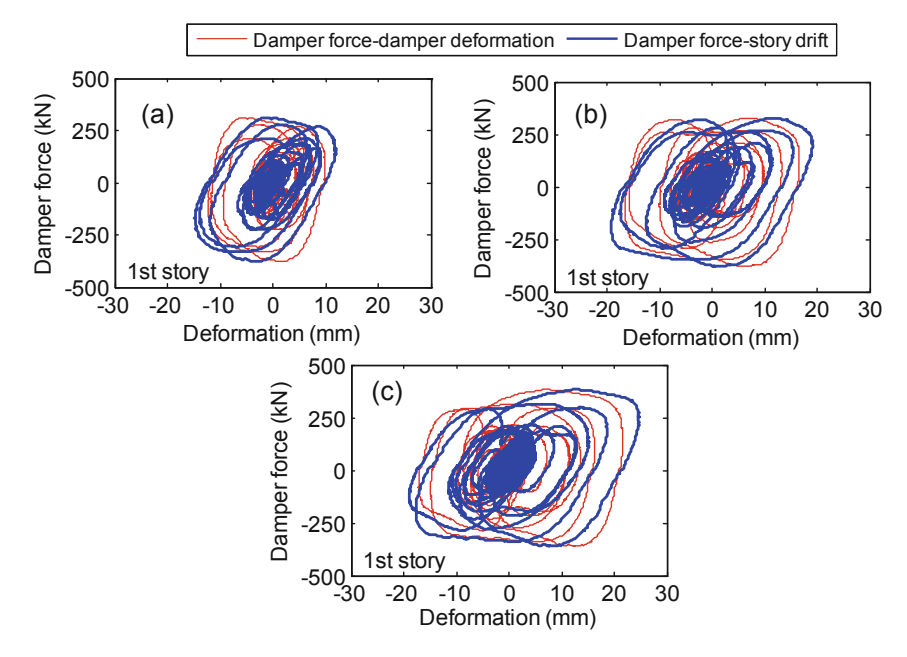


Fig. 24. Damper force-deformation response from DBE level RTHS with HECTOR-11625090 record level: (a) D100V; (b) D75V; and (c) D60V, (after Dong et al. [24]).

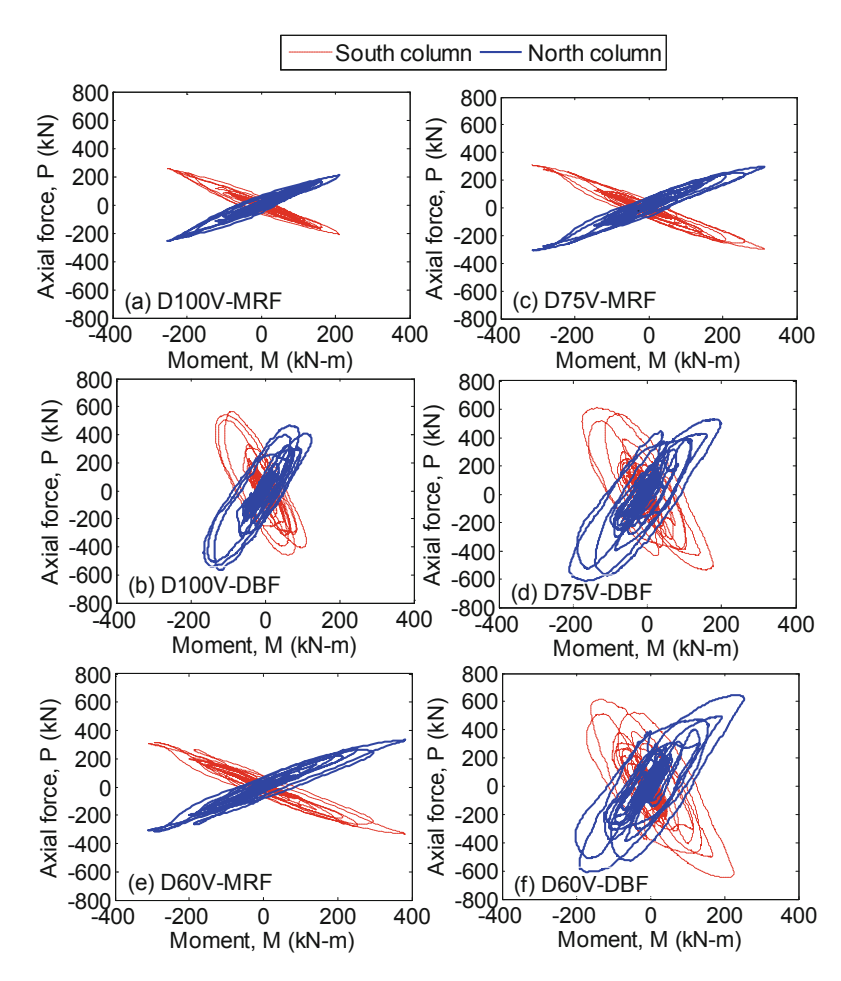


Fig. 25. Axial force-bending moment response for 1st story columns from DBE level RTHS with HECTOR-11625090 record, (after Dong et al. [24]).

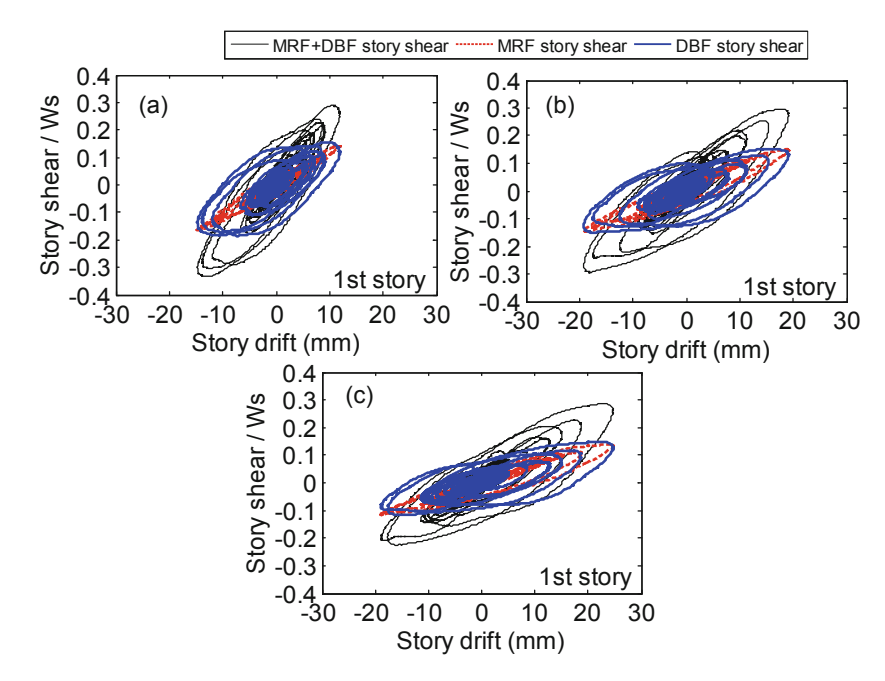


Fig. 26. Story shear force in DBE level RTHS with HECTOR-11625090 record: (a) D100V (Ws = 2702 kN); (b) D75V (Ws = 3603 kN); (c) D60V (Ws = 4504 kN), (after Dong et al. [24]).

Figures 27 and 28 show the probabilities of exceedance (POEs) for the peak story drift ratios of each test structure under the DBE and MCE ground motions, respectively. In these figures the data points are the POE calculated directly from the RTHS results. The continuous line is a lognormal distribution fit to the data points. The lognormal distribution fits the data well, indicating that the story drift ratios can be assumed to be lognormally distributed. Accordingly, the probability of the peak story drift ratio exceeding the limit for a certain performance level can be estimated. The POEs for the Immediate Occupancy performance level story drift limit (0.7% rad) for the D100V, D75V, and D60V structures under the DBE are 68, 97, and 99%, respectively; however, the POEs for the Life Safety performance story drift limit (2.5%) rad) under the DBE are less than 1%. The POEs for the Life Safety performance level story drift limit (2.5% rad) under the MCE are 4 and 14% for the D75V and D60V structures, respectively, and much less than 1% for the D100V structure. The POEs for the Collapse Prevention performance level story drift (5.0% rad) for all the structures under the MCE are much less than 1%, indicating a very low probability of collapse even for the structures with a reduced base shear design strength. For example, for the D60V structure, the 1% POE value of the peak story drift ratio is 2.9% rad, which is much less than the 5.0% rad limit for the Collapse Prevention performance level.

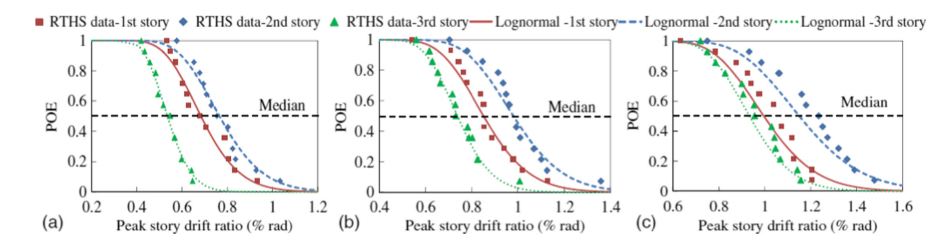


Fig. 27. Probability of exceedance (POE) for peak story drift ratio under DBE RTHS: (a) D100V; (b) D75V; (c) D60V, (after Dong et al. [24]).

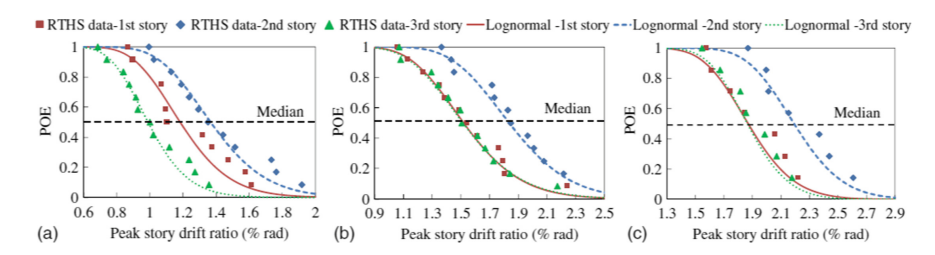


Fig. 28. Probability of exceedance (POE) or peak story drift ratio under MCE RTHS: (a) D100V; (b) D75V; (c) D60V (after Dong et al. [24]).

The frequency response transfer function (FRF) between the structural response during a RTHS and the ground motion input were determined and used to estimate the first mode natural frequency and equivalent damping ratio provided by the dampers for each test structure. The FRF is calculated as the quotient of the fast Fourier transform (FFT) of the output over the FFT of the input. One FRF is calculated for each RTHS, where the input is the ground acceleration and the output is the total floor acceleration of the third floor. For each test structure, an ensemble of FRFs was generated for the DBE ground motion ensemble, and another ensemble of FRFs was generated for the MCE ground motion ensemble. The mean FRF of each ensemble of FRFs was used to estimate the natural frequency and equivalent damping ratio of the test structure. Figure 29 shows the amplitude of the mean FRF versus the frequency for each test structure for the DBE and MCE ground motion ensembles. The first mode natural frequency of each test structure was estimated as the frequency corresponding to the peak amplitude, and the total equivalent (first mode) damping ratio corresponding to the peak was estimated using the half-power bandwidth method [55]. The estimated total equivalent damping ratio was taken as ξt, which is the sum of the equivalent damping ratio provided by the dampers, ξe , plus the inherent damping ratio of the building (which represents other energy dissipation within the building during lowamplitude dynamic response). Le was estimated by subtracting the assumed inherent damping ratio of the building (2%, which was included in the analytical substructure in the RTHS) from the estimated \(\xi\$t. The estimated \(\xi\$e values for the D100V, D75V, and D60V test structures are 29, 32, and 31% for the DBE ground motions and 37, 31, and

31% for the MCE ground motions, respectively. These results show that the nonlinear viscous dampers provided large energy dissipation capacity to the test structures (see Table 9).

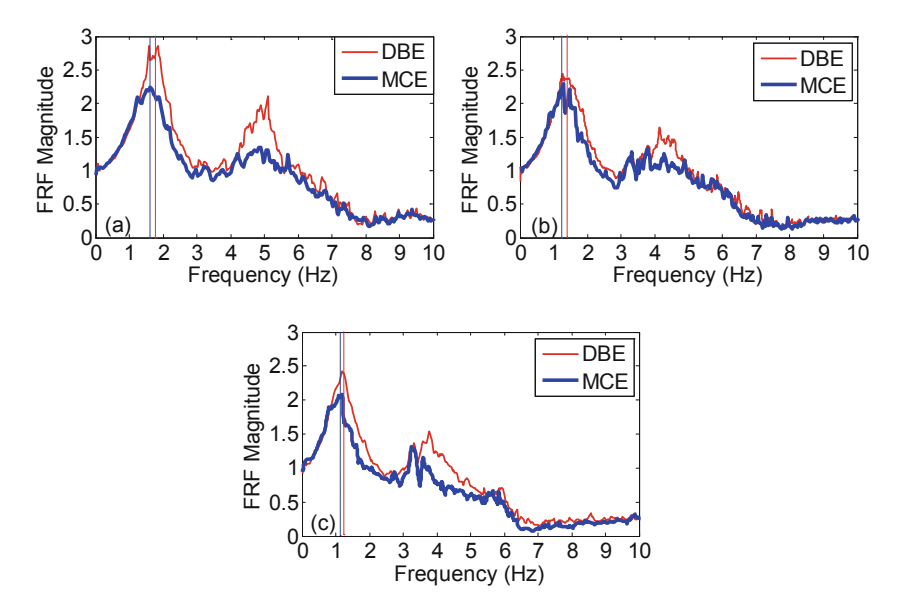


Fig. 29. Magnitude of frequency response function of test structures: (a) D100V; (b) D75V; (c) D60V, (after Dong et al. [24]).

Structure	DBE		MCE	MCE			
	Natural frequency	Equivalent	Natural frequency	Equivalent			
	(1st mode, Hz)	damping ratio	(1st mode, Hz)	damping ratio			
		ξe		ξe			
D100V	1.70	29%	1.63	37%			
D75V	1.45	32%	1.35	31%			
D60V	1.24	31%	1.19	31%			

Table 9. Estimated natural frequency and damping ratio of test structure.

The RTHS method enabled a comprehensive study to be performed which investigated the behaviour of nonlinear viscous dampers and their interaction with structural systems during strong earthquake ground motions. In conclusion, the experimental study showed that: (1) elastic flexibility in the damper force path in a practical steel frame building structure, along with the nonlinearity of a typical nonlinear viscous damper, causes the viscous damper forces to be partially in phase with the story drifts; (2) the in-phase damper force behavior results in a combined column response with large axial force at the time of peak bending moment, and these combined column

demands should be considered in the design of frames with nonlinear viscous dampers; (3) the in-phase damper force behavior stiffens the steel frame building structure and reduces the story drifts relative to design predictions; and (4) an MRF building structure with nonlinear viscous dampers can be designed with a reduced MRF base shear design strength and still achieve high performance between immediate occupancy performance and life safety performance under MCE ground motions, as well as a low probability of collapse based on the peak story drift response and a high probability of good post-earthquake functional performance based on the residual story drift response under MCE ground motions.

3.3 Tall Buildings with Damped Outrigger Systems

With the quest to construct taller buildings in earthquake-prone regions, the seismic performance of such structures is of considerable interest. To protect structural systems from earthquake and wind hazards, researchers and engineers have developed several passive, semi-active, and active control devices to improve the system's performance. A study was therefore undertaken to investigate the seismic performance of tall buildings outfitted with an outrigger system with supplemental nonlinear viscous dampers. The purpose for the supplemental dampers was to improve the seismic response of the building to strong ground motions, while also reducing the floor accelerations from wind loading. Only the study related to earthquake loading is presented herein.

A 44-story steel building is used in this study that is part of the California Tall Building Initiative [56] conducted by the PEER Center. The prototype building is shown in Fig. 30. It is located in Los Angeles, California and has a height of 166 m and a footprint of 51.8 by 32.6 m, with four stories below the ground level. Six buckling restrained braced frames (BRBF) are located in the E-W and N-S directions to resist lateral loads. The braces have a yieldable core of 70% of their brace length. The columns are constructed of steel tubes filled with concrete. The beams are wide flange steel sections with gravity connections at their ends. Outrigger trusses are located at the 20th, 30th, and 40th stories in the N-S direction and extend from the core to outrigger columns located at the four corners of the building. The original design of the building had the outriggers pinned to the perimeter columns [56]. In the current study the design is modified to include nonlinear viscous dampers placed between the end of each outrigger truss and the perimeter columns, similar to that proposed in [57], resulting in adding dampers at 12 different locations of the building [58]. The building was originally designed with the seismic performance objectives that include drift limits of 0.5% under the serviceability limit earthquake and 3% under the MCE, respectively, in accordance with ASCE 7-05 [59].

The building has a period of 6.2 s and 5.0 s for modes 1 and 2, which are translational modes in the NS and EW directions. Mode 3 is a torsional mode with a 3.2 s period.

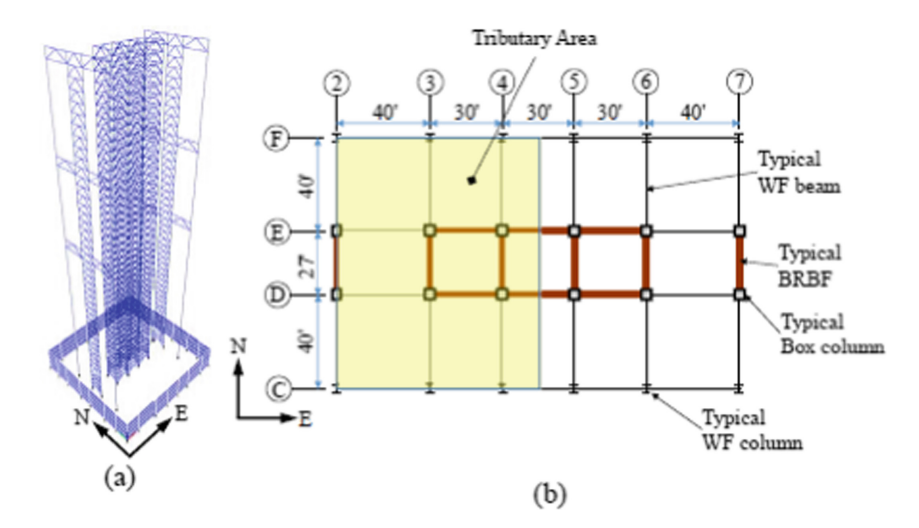


Fig. 30. Prototype building: (a) 3D view, and (b) floor plan (outrigger not shown for clarity in the floor plan) Note 1 ft. = 0.3048 m.

Real-Time Hybrid Simulation Configuration. Figure 31 shows the real-time hybrid simulation configuration for the tall building study. The building is modelled numerically via an analytical substructure while one nonlinear viscous damper is modelled physically in the laboratory using an experimental substructure. The remaining dampers are modelled numerically using on-line model updating [30] and included in the analytical substructure. The analytical substructure is created using the finite element method. The earthquake ground accelerations are applied to the structure as an effective force over the height of the building. By solving the equations of motion in real-time, the command displacement to the actuator is calculated and imposed onto the experimental substructure to capture the rate dependency of the nonlinear viscous damper. The measured damper force along with the computed member forces of the analytical model are used as a restoring force to integrate the equations of motion using the MKR- α algorithm [12]. The response of the analytically modelled nonlinear viscous dampers at other locations of the building is performed using an explicit non-iterative nonlinear Maxwell Model formulation that enables performing the state determination of the model in real-time [30]. The parameters of the analytically modelled dampers are obtained based on the measured response of the physical damper and model updating using the unscented Kalman filter [60]. These identified parameters are used to predict the damper response at other locations of the building in each time step of the RTHS. The RTHS used a time step of $\Delta t = 6/1024$ s, with $\rho_{\infty} = 0.50$. Convergence studies were performed to ensure that using $\Delta t = 6/1024$ s provided accurate results. The ATS compensator was used for the RTHS. As in the RTHS of the three-story building described in the previous section, the root mean square (RMS) over a one second window of the actuator command was used to activate and deactivate the ATS

coefficient updating for the tall building RTHS. When the RMS value was about 1 mm the ATS was triggered, and turned off when below the 1 mm RMS value.

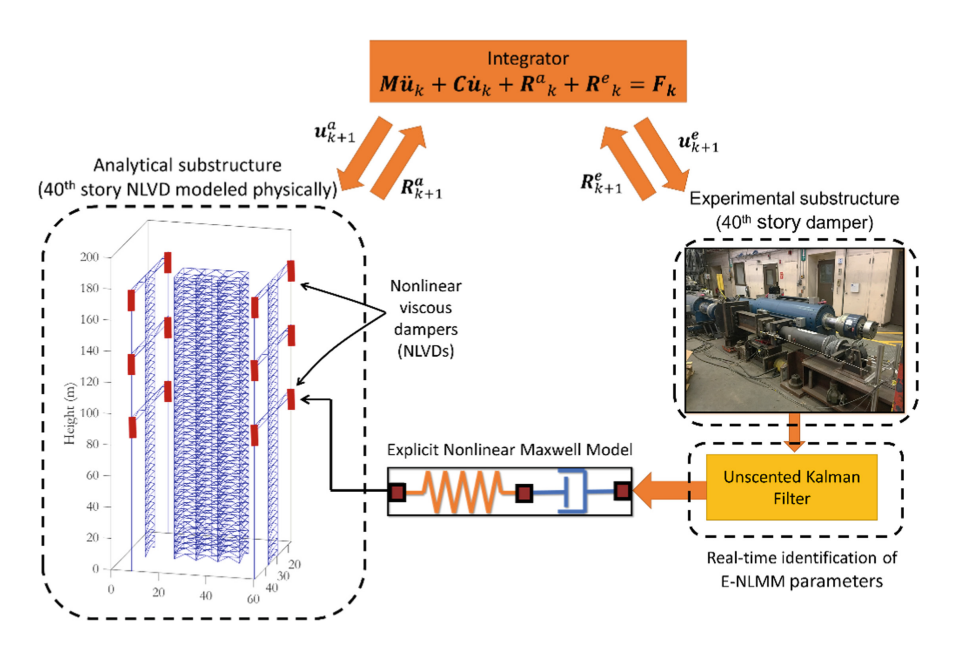


Fig. 31. Schematic of real-time hybrid simulation configuration with on-line model updating.

Analytical Substructure for the Real-Time Hybrid Simulation. A 3-D analytical model of the building is created using the HyCoM-3D software [61], and is shown in Fig. 31. The columns and beams are modelled using elastic beam-column elements, while the buckling restrained braces are modelled using nonlinear truss elements. A lean-on column is placed at the center of each floor where its node is considered as the master node of the floor level. All other nodes at each floor level are slaved to their master node to simulate rigid floor diaphragms. The column nodes at the ground level are restrained in both horizontal directions to simulate the restraint provided by the foundation. At each floor level the mass is lumped at the master node, and includes translation mass in both horizontal directions and torsion rotational inertia associated with the distributed floor mass. The resulting analytical substructure model included 3,974 degrees of freedoms, which is challenging to run in real-time. Therefore, a super element is used to condense all linear elements in the model, namely the beams and columns, resulting in 1,428 degrees of freedom while enabling the nonlinear behavior of the BRBFs and outrigger trusses of the building to be captured. The beams and columns of the building are expected to be free from damage under earthquakes, thus making it appropriate to model them using linear elastic elements.

The analytically modelled dampers in the model are based on the explicit nonlinear Maxwell Model (E-NLMM) which provides an explicit non-iterative solution of the constitutive relations [30]. The unscented Kalman filter (UKF) is used to identify the model parameters of each damper in real time based on the response of the experimentally modelled damper. The initial mean of the state variables for the dashpot coefficient C_d , stiffness K_d , and exponent α of the E-NLMM used by the UKF are 90,800 kN/m, 671 kN.(s/m) $^{\alpha}$ and 0.45, respectively. The measurement noise is a Gaussian random variable with a mean of 0 kN and standard deviation of 8 kN. Additional details are found in [30].

Experimental Substructure for the Real-Time Hybrid Simulation. The experimental substructure for the RTHS includes a full scale nonlinear viscous damper manufactured by Taylor Device Inc. having a 600 kN capacity and ± 125 mm stroke. The damper is connected to a 1,700 kN dynamic hydraulic actuator via a load transfer beam and a load cell. The experimental substructure physically models the damper located at the N-W corner of the 40^{th} story between the end of the outrigger truss and the perimeter column. Since four parallel dampers are placed between the perimeter column and truss at each location, the measured damper force is multiplied by a factor of four to simulate four identical dampers acting in parallel.

Ground Motion Selection and Scaling. The two horizontal components of the 1989 Loma Prieta earthquake ground motion recorded at the Saratoga Aloha Avenue Station are used in the RTHS presented herein. The California Tall Building Initiative selected seven ground motions to study the seismic response where the Loma Prieta ground motion is one of these. Following the ground motion scaling procedure laid out in the California Tall Building Initiative case studies [56], the records are scaled to the target uniform hazard spectrum for the MCE hazard level over a period range of interest. The scaling factor for the Loma Prieta ground motion is 1.89 [29, 56]. Additional RTHS were performed using the complete ensemble of ground motions and presented in [62].

Real-Time Hybrid Simulation Results. Figure 32 shows the time history roof displacements in the E-W and N-S directions from the RTHS with dampers. The peak roof displacement is greater in the E-W direction compared to the N-S direction, where the latter is associated with the plane of the outriggers. The force-deformation hysteretic response of the bucking restrained braces at the 1st story orthogonal BRBFs are included in Fig. 32. The E-W brace exhibited greater deformations with a ductility of 3.0 compared to a value of 2.0 in the N-S brace. The damper force-deformation hysteretic response is also shown in Fig. 32, where the force capping due to the high velocity in the nonlinear viscous damper is evident in the figure. The peak lateral floor displacements along the height of the building is shown in Fig. 33 where it is compared with the base case simulation (i.e., no dampers in the outriggers). A reduction is shown to occur in the peak floor displacement in the N-S direction when the dampers are added. The reduction ranges from 3.3% at story 22 to 18% at story 28. The dampers do not appear to improve the building response in the E-W direction.

The response of the dampers at the 40th story is shown in Fig. 34 where the N-W damper is physically modelled. The time histories of the identified damper parameters are shown in Fig. 35, where the parameters are normalized by their initial values. These parameters are used to predict the response of the 11 other dampers, including the N-E, S-W, and S-E corners at the 40th story whose results (N-E, S-W, and S-E corners) are shown in Fig. 35. The model parameters of the analytically modelled dampers are shown to vary over the course of the simulation, which illustrates the importance of using on-line model updating to obtain an accuracy response prediction.

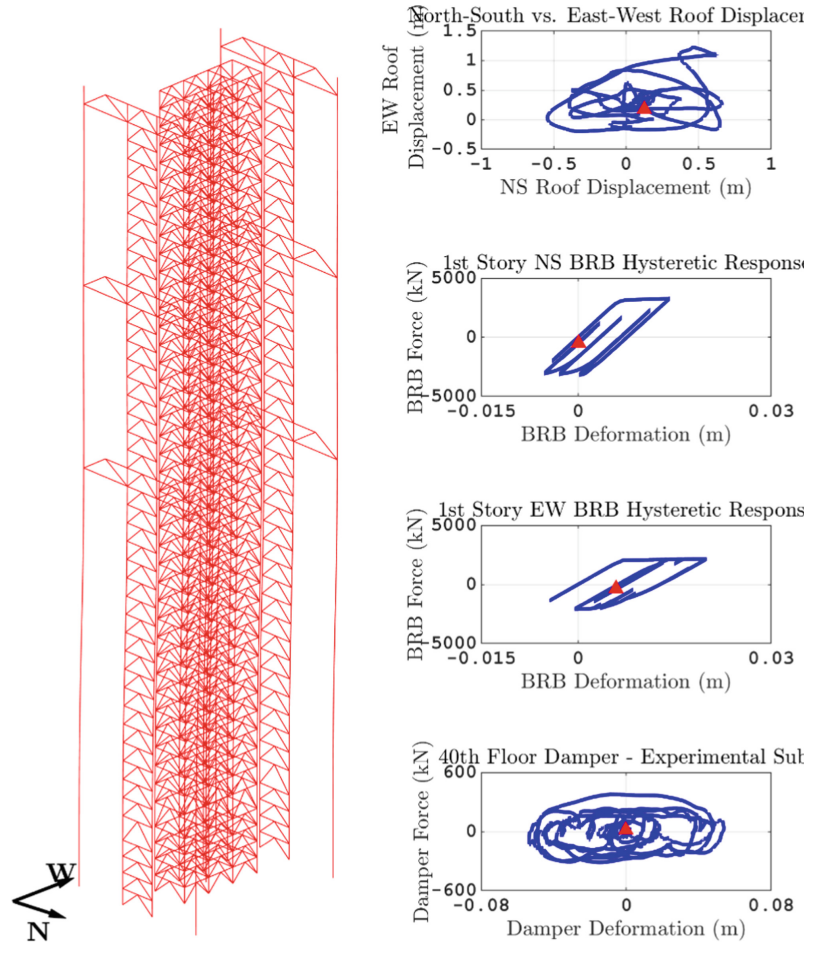


Fig. 32. Real-time hybrid simulation results.

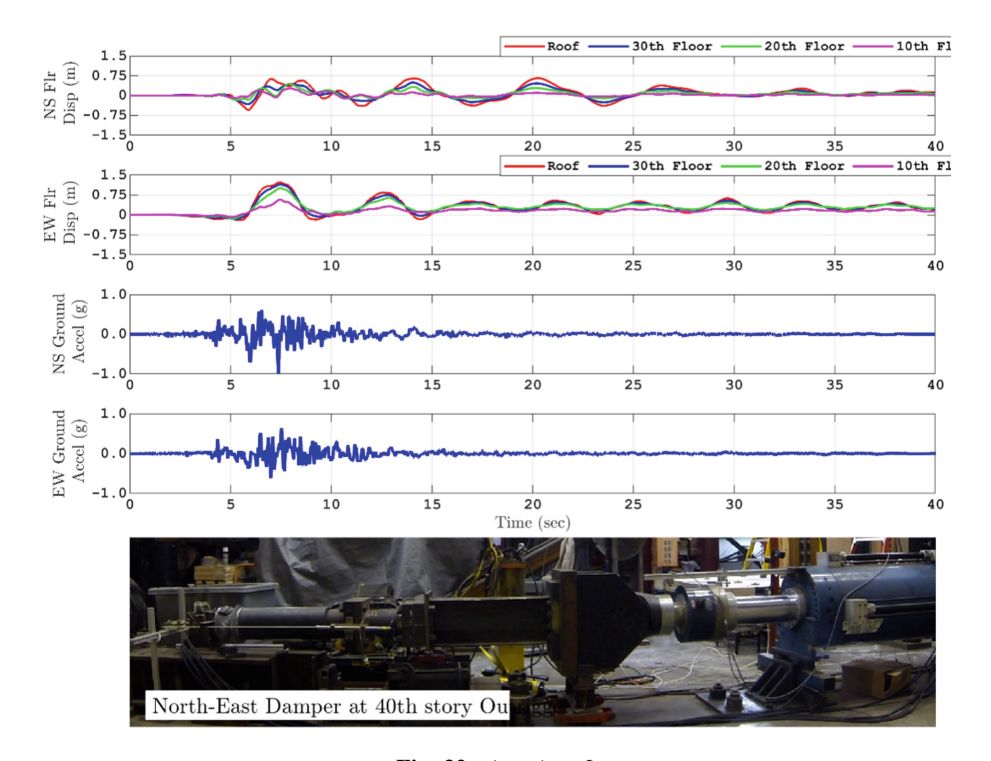


Fig. 32. (continued)

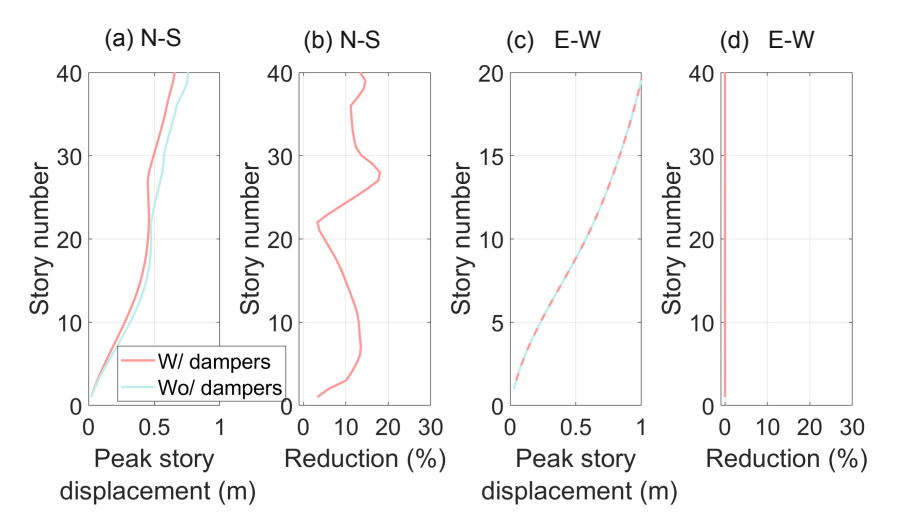


Fig. 33. Peak lateral floor displacements and associated reduction.

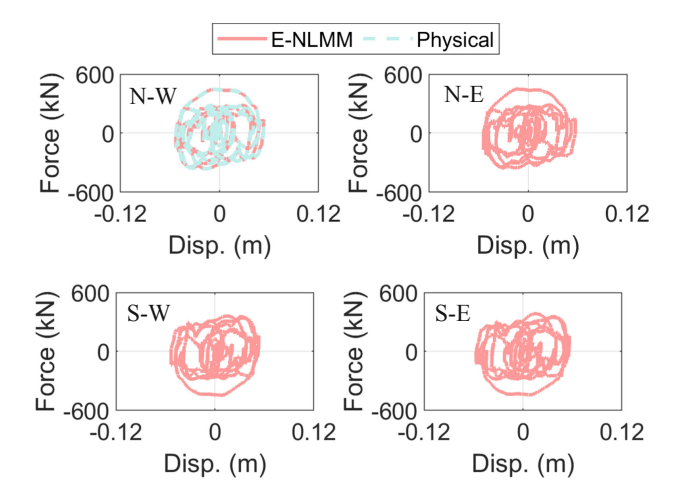


Fig. 34. Response of dampers at the four corners of the 40th story

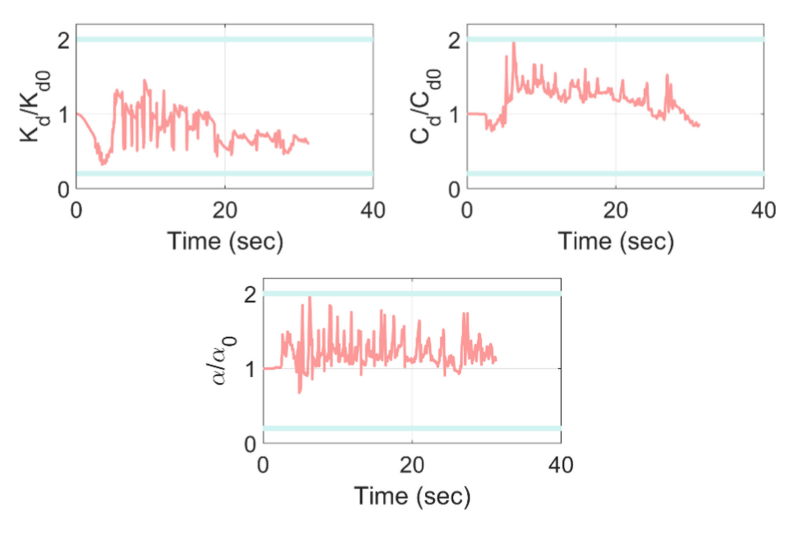


Fig. 35. Identified parameters of the explicit nonlinear Maxwell model along with their ceiling limits.

The performance of the ATS compensator was found to be exceptional in imposing accurate actuator motions to the experimental substructure. Figure 36 shows the synchronization subspace plot that compares the measured damper displacement x^m with the target displacement x^l from the integration of the equations of motion. The normalized RMS error (NRMSE) was 0.12%, which is small and illustrates that accurate motions without amplitude or delay errors took place during the RTHS. The time histories of the ATS adaptive coefficients are shown in Fig. 37, where they are seen to vary in time in order to achieve accurate actuator control. The coefficient a_0 is seen to

vary from 0.98 to 1.01, indicating that a minimal amount of amplitude correction was performed. The coefficient a_1 is seen to also vary in time, where the compensation for time delay, τ_k , ranges from about 0.016 to 0.024 s. As already mentioned, the time step used in the RTHS was $\Delta t = 6/1024$ s, and hence the delay compensation represents a significant amount of correction that is necessary to achieve accurate RTHS.

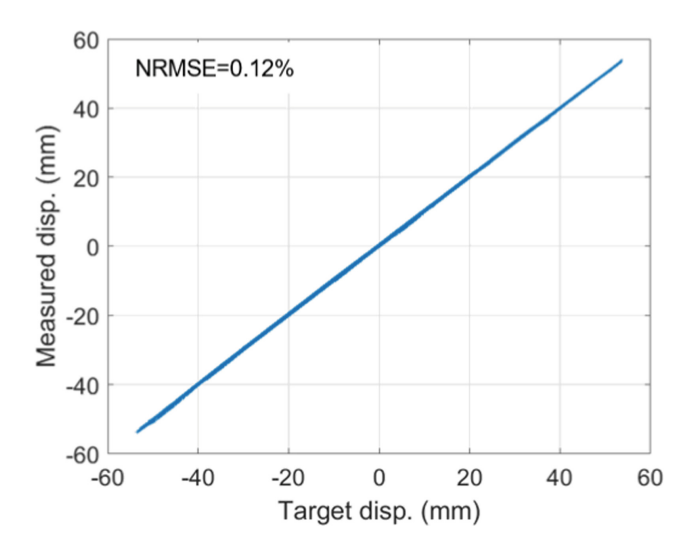


Fig. 36. Synchronization subspace plot showing targeted vs. measured actuator displacement, at 40^{th} story N-W corner damper.

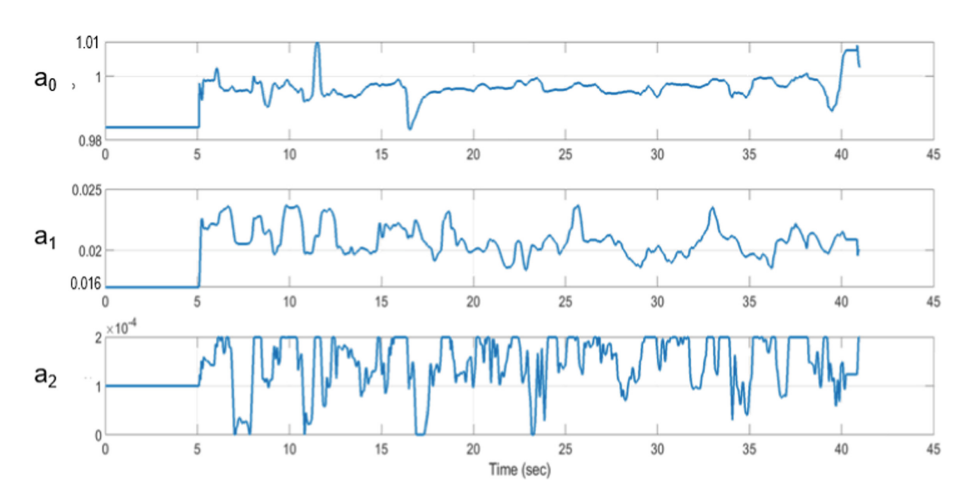


Fig. 37. Time history of ATS Compensator adaptive coefficients, 40th story damper.

The force path associated with the damper force must be considered in designing the damper system. As found in the 3-story building with MRFs and DBFs presented earlier, the elastic flexibility of members in the force path of the dampers can have a significant effect on the response of the structure, and thereby the effectiveness of the dampers in reducing the motions of the structure. The outrigger trusses and outrigger columns are in the direct force path of the damper forces. To investigate the effect of elastic flexibility of members in the force path of the dampers, the stiffness of the outrigger system (the outrigger trusses and outrigger columns) and the number of dampers at each floor were systematically varied and a series of RTHS were performed. The results of the study are shown below in Fig. 38, where the maximum floor accelerations are plotted as a function of the variation of outrigger stiffness and number dampers. Results are shown for the 20th, 30th, and 40th floor, where the outrigger trusses exist in the building. The nomenclature for the number of dampers is associated with the total number of dampers placed at the ends of the outrigger trusses at the 20th, 30th, and 40th floors, respectively, (e.g., Case 2 implies 2 parallel dampers at the end of each outrigger). The results shown in Fig. 38 are associated with wind loading applied to the building, and were found to correlate to earthquake loading as well.

Figure 38(a) shows that increasing the stiffness multiplier applied to the members of the outrigger system to a value of three leads to an appreciable reduction in the maximum accelerations at the 20^{th} , 30^{th} , and 40^{th} floors compared to the as-built structure (i.e., a rigid connection with no dampers between the ends of the outrigger trusses and outrigger columns). A larger reduction in maximum floor accelerations occurs in the 30^{th} and 40^{th} floors compared to the 20^{th} floor. For a stiffness multiplier value of three, the reduction in maximum acceleration is 23%, 32%, and 37% at the 20^{th} , 30^{th} , and 40^{th} floors, respectively, compared to the as-built structure. Any further increase in the stiffness multiplier value is shown to offer little additional reduction in the maximum floor accelerations. The stiffness multiplier-maximum acceleration relationship shown in Fig. 38(a) remains nearly constant when the stiffness multiplier is increased to a value larger than three.

Figure 38(b) shows that the number of dampers affects the amount of reduction in the maximum floor acceleration. Similar to the stiffness multiplier results for reduction in maximum acceleration, there is a limit to the number of dampers beyond which there is a minimal benefit of adding more dampers. It appears that the number of dampers associated with Case 3 (i.e., a total of 3 parallel dampers are added at the end of each outrigger truss) appears to be ideal in reducing the maximum floor accelerations. For this case, the maximum acceleration reduction is 29%, 29%, and 36% at the 20^{th} , 30^{th} , and 40^{th} floors, respectively. For Case 3, FRFs were obtained using RTHS to estimate the equivalent damping ratio provided by the dampers, ξ_e . It was determined that the equivalent damping under DBE ground motions is about 16% in the first mode of vibration, which is a translational mode in the plane of the outrigger trusses (i.e., in the N-S direction, see Fig. 32).

Overall, there does not appear to be a need to increase the stiffness of the outrigger truss and column members by more than a factor of three in order to limit the deformations in these members and instead collect deformations in the dampers to dissipate energy. This result is significant when outfitting the building with dampers since it is impractical to markedly increase the stiffness of the outrigger truss and column

members, which would result in the member cross-sectional dimensions potentially becoming extremely large. In addition, adding too many dampers can be ineffective, as the velocity in the dampers is reduced leading to a reduced efficiency of each damper and total energy dissipation.

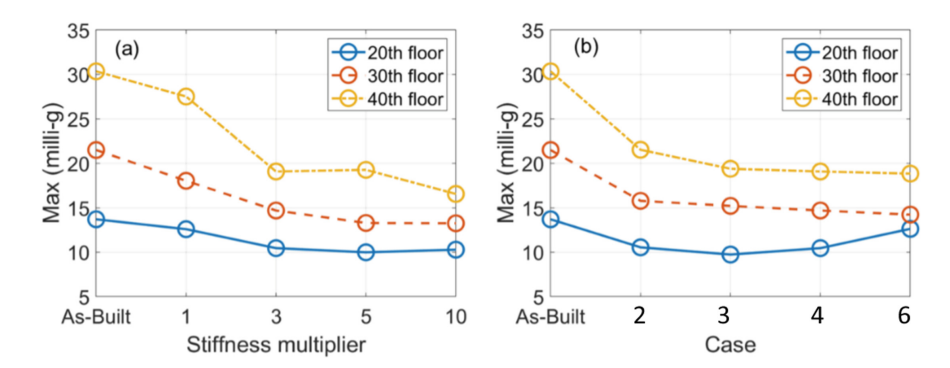


Fig. 38. Maximum floor accelerations: (a) effect of stiffness multiplier for damper Case 4; and (b) effect of the number of dampers for a stiffness multiplier of 3.

An examination of the frequency decomposition of the roof displacement from the RTHS involving seismic loading (not shown herein) indicated that the building's response included both translation and torsional modes. The translation modes in the N-S direction however were the only modes that contributed to the damper deformations.

The results from the RTHS show that an damped outrigger system has potential in mitigating seismic hazards in tall buildings. To investigate the effects of adding nonlinear viscous dampers to the outrigger system, it was necessary to perform RTHS. Attempting to perform a pure numerical study would likely lead to inaccuracies in the results, for the RTHS showed that the coefficients of numerical models of the dampers are not constant, and that they varied during the earthquake. The RTHS enabled the modeling of the dampers to be accurately performed, using an experimental substructure with a nonlinear viscous damper to conduct on-line model updating of other dampers in the building that were numerically modelled. The integration algorithm enabled the equations of motion to be integrated in an explicit, numerically stable manner. The dissipative characteristics of the MKR- α Method damped out the spurious high frequency noise in the system without affecting the modes of interest, where the noised is caused by a change of state (i.e., nonlinear behavior) of the BRBs within a time-step [9, 10, 12]. The RTHS configuration permitted a series of simulations to be readily performed in order to systematically investigate the effects of various parameters on the performance of the building. This was enabled by reinitializing the analytical substructure to its initial state and returning the damper to its initial unstressed condition at the beginning of each simulation.

4 Summary and Conclusions

This paper presented the concept of RTHS and developments achieved at the NHERI Lehigh Experimental Facility that have advanced RTHS to readily enable accurate large-scale, multidirectional earthquake simulations to be performed. Recent advancements in RTHS at the Lehigh NHERI Experimental Facility presented include the development of dissipative explicit direct integration algorithms that are unconditionally stable and well suited for RTHS with nonlinear geometric and material nonlinearities. Additional developments include the formulation of explicit force-based fiber elements that are ideal for the real-time state determination of the analytical substructure where nonlinear computational models are involved. Advancements were also presented that include adaptive control to enable precise real-time control of servohydraulic actuators in test setups for a RTHS experimental substructure.

The use of these advancements enables robust testing of structural components and systems to be conducted, where the effects of interactions of components with members of the system, soil-structure interaction, and fluid-structure interaction can be rigorously investigated. RTHS enables the hazard level for the experiment to be readily defined. Moreover, the method fulfils the need of a framework that can comprehensively validate design procedures of a structural system to achieve high performance objective levels for prescribed hazard levels.

Acknowledgments. The research and testing presented herein were performed at the Lehigh NHERI Experimental Facility, whose operation has been supported by grants from the National Science Foundation (NSF) under Cooperative Agreement No. CMS-0402490 and Cooperative Agreement No. CMMI-1520765. The NHERI Lehigh Experimental Facility is led by Professor James Ricles (Director), Professor Richard Sause (Co-Director), Dr. Chad Kusko (Operations Manager), Thomas Marullo (IT Systems Administrator and Research Scientist), and Dr. Liang Cao (Research Scientist). The research projects reported herein were funded by NSF under Grant No. CMS-0420974, within the George E. Brown, Jr. Network for Earthquake Engineering Simulation Research (NEESR) Program, Award No. CMS- 0936610 in the George E. Brown, Jr. NEESR program, and CMMI Award No. 1463497. Support was also provided by the Pennsylvania Department of Community and Economic Development through the Pennsylvania Infrastructure Technology Alliance. Taylor Device Inc. is also acknowledged for providing the nonlinear fluid viscous dampers used in this research. The opinions expressed in this paper are those of the authors and do not necessarily reflect the views of the sponsors.

The author would like to acknowledge the technical support provided by the staff of the Lehigh NHERI Experimental Facility, including Thomas Marullo and Darrick Fritchman. Numerous former and current students have all made significant contributions to the research reported herein. They include (in random order): Dr. Chinmoy Kolay; Dr. Yunbyeong Chae; Dr. Cheng Chen; Dr. Baiping Dong; Dr. Ricardo Herrera, Dr. Brent Chancellor, Dr. David Roke, Dr. Theodore Karavasilis; Dr. Oya Mercan, Dr. Liang Cao, Dr. Choung-Yeol Seo, and Safwan Al-Subaihawi.

Finally, the author would like to acknowledge Richard Sause, the Joseph T. Stuart Professor of Structural Engineering, ATLSS Center Director at Lehigh University, and co-Director of the Lehigh NHERI Experimental Facility. Professor Sause and the author have collaborated together for over 30 years. His encouragement, collaboration, and major contributions to the research presented herein are greatly appreciated and for which the author is deeply indebted.

References

- Okazaki T, Lignos DG, Midorikawa M, Ricles JM, Love J (2013) Damage to steel buildings observed after the 2011 Tohoku Earthquake. Earthq Spectra EERI 29:219–243
- Okawa I, Kashima T, Koyama S, Iiba M (2013) Recorded responses of building structures during the 2011 Tohoku-Oki Earthquake with some implications for design practice. Earthq Spectra EERI 29:245–264
- Kasai K, Mita A, Kitamura H, Matsuda K, Morgan T, Taylor A (2013) Performance of seismic protection technologies during the 2011 Tohoku-Oki Earthquake. Earthq Spectra EERI 29:265–293
- 4. Moon L et al (2014) The demise of the URM building stock in Christchurch during the 2010–2011 Canterbury Earthquake sequence. Earthq Spectra EERI 30:253–276
- Galloway B, Hare J, Brunsdon D, Wood P, Lizundia B, Stannard M (2014) Lessons from the post-earthquake evaluation of damaged buildings in Christchurch. Earthq Spectra EERI 30:451–474
- Chang S, Taylor J, Elwood K, Seville E, Brunsdon D, Gartner M (2014) Urban disaster recovery in Christchurch: the Central Business District Cordon and other critical decisions. Earthq Spectra EERI 30:513–532
- 7. Nakashima M, Kato H, Takaoka E (1992) Development of real-timepseudodynamic. Testing Earthq Eng Struct Dyn 21(1):79–92
- Kolay C, Ricles JM (2016) Assessment of explicit and semi-explicit classes of model-based algorithms for direct integration in structural dynamics. Int J Numer Methods Eng 107:49– 73. https://doi.org/10.1002/nme.5153
- Kolay C, Ricles J (2014) Development of a family of unconditionally stable explicit direct integration algorithms with controllable numerical energy dissipation. Earthq Eng Struct Dyn 43(9):1361–1380. https://doi.org/10.1002/eqe.2401
- Kolay C, Ricles J, Marullo T, Mahvashmohammadi A, Sause R (2015) Implementation and application of the unconditionally stable explicit parametrically dissipative KR-α method for real-time hybrid simulation. Earthq Eng Struct Dyn 44(5):735–755. https://doi.org/10.1002/ eqe.2484
- 11. Chung J, Hulbert G (1993) A time integration algorithm for structural dynamics with improved numerical dissipation: the generalized-alpha method. J Appl Mech 60(2):371–375. https://doi.org/10.1115/1.2900803
- Kolay C, Ricles J (2019) Improved explicit integration algorithms for structural dynamic analysis with unconditional stability and controllable numerical dissipation. J Earthq Eng 23 (5):771–792. https://doi.org/10.1080/13632469.2017.1326423
- 13. Spacone E, Ciampi V, Filippou F (1996) Mixed formulation of nonlinear beam finite element. Comput Struct 58(1):71–83
- Kolay C, Ricles J (2017) Force-based frame element implementation for real-time hybrid simulation using explicit direct integration algorithms. J Struct Eng 144(2):04017191. https://doi.org/10.1061/(ASCE)ST.1943-541X.0001944
- 15. OpenSees [Computer software] (2017) Pacific Earthquake Engineering Research Center, University of California, Berkeley, CA
- Chae Y, Kazemibidokhti K, Ricles J (2013) Adaptive time series compensator for delay compensation of servo-hydraulic actuator systems for real-time hybrid simulation. Earthq Eng Struct Dyn 42(11):1697–1715. https://doi.org/10.1002/eqe.2294
- 17. Horiuchi T, Konno T (2001) A new method for compensating actuator delay in real-time hybrid experiments. Philos Trans R Soc Lond Ser A 359:1786–1893

- 18. Lamarche C, Tremblay R, Leger P, Leclerc M, Bursi O (2010) Comparison between realtime dynamic substructuring and shake table testing techniques for nonlinear seismic applications. Earthq Eng Struct Dyn 39:1299–1320
- 19. Ahmadizadeh M, Mosqueda G, Reinhorn A (2008) Compensation of actuator delay and dynamics for real-time hybrid structural simulation. Earthq Eng Struct Dyn 37:21–42
- Phillips B, Spencer B (2012) Model-based feedforward-feedback actuator control for realtime hybrid simulation. ASCE J Struct Eng 139:1205–1214. https://doi.org/10.1061/(ASCE) ST.1943-541X.0000606
- Cao L et al (2020) NHERI Lehigh Experimental Facility with large-scale multi-directional hybrid simulation testing capabilities. Front Built Environ - Wind Eng Sci 6:107. https://doi. org/10.3389/fbuil.2020.00107
- 22. Matlab (2022) A registered trademark of The Math Works, Inc. http://www.mathworks.com
- Dong B, Sause R, Ricles JM (2015) Accurate real-time hybrid earthquake simulations on large-scale MDOF steel structure with nonlinear viscous dampers. Earthq Eng Struct Dyn 44 (12):2035–2055. https://doi.org/10.1002/eqe.2572
- Dong B, Sause R, Ricles JM (2016) Seismic response and performance of a steel MRF building with nonlinear viscous dampers under DBE and MCE. J Struct Eng 142 (6):04016023. https://doi.org/10.1061/(ASCE)ST.1943-541X.0001482
- Dong B, Sause R, Ricles JM (2018) Seismic response and damage of reduced-strength steel MRF structures with nonlinear viscous dampers. J Struct Eng 144(12):2035–2055. https://doi.org/10.1061/(ASCE)ST.1943-541X.0002226
- Chae Y, Ricles JM, Sause R (2013) Large-scale experimental studies of structural control algorithms for structures with magnetorheological dampers using real-time hybrid simulation. J Struct Eng 139(7):1215–1226. https://doi.org/10.1061/(ASCE)ST.1943-541X. 0000691
- Chae Y, Ricles J, Sause R (2014) Large-scale real-time hybrid simulation of a 3-story steel frame structure with magneto-rheological dampers. Earthq Eng Struct Dyn 43(13):1915– 1933. https://doi.org/10.1002/eqe.2429
- 28. Al-Subaihawi S, Kolay C, Marullo T, Ricles J, Quiel S (2020) Assessment of wind-induced vibration mitigation in a tall building with damped outriggers using real-time hybrid simulations. Eng Struct 205:110044. https://doi.org/10.1016/j.engstruct.2019.110044
- 29. Kolay C, Al-Subaihawi S, Marullo T, Ricles J, Quiel S (2020) Multi-hazard real-time hybrid simulation of a tall building with damped outriggers. Int J Lifecycle Perform Eng 4 (1/2/3):103–132. https://doi.org/10.1504/IJLCPE.2020.108937
- Al-Subaihawi S, Ricles JM, Quiel SE (2022) Online explicit model updating of nonlinear viscous dampers for real time hybrid simulation. Soil Dyn Earthq Eng 154:107108. https:// doi.org/10.1016/j.soildyn.2021.107108
- 31. Lin YC, Sause R, Ricles JM (2013) Seismic performance of a steel self-centering. Moment resisting frame: hybrid simulations under design basis earthquake. J Struct Eng ASCE 139 (11):1823–1832. https://doi.org/10.1061/(ASCE)ST.1943-541X.0000745
- 32. Ricles JM, Sause R, Garlock M, Zhao C (2001) Post-tensioned seismic resistant connections for steel frames. J Struct Eng ASCE 127(2):113–121
- 33. Ricles JM, Sause R, Peng SW, Lu LW (2002) Experimental evaluation of earthquake resistant posttensioned steel connections. J Struct Eng 128(7):850–859. https://doi.org/10.1061/(ASCE)0733-9445(2002)128:7(850)
- 34. Garlock M, Ricles JM, Sause R (2005) Experimental studies on full-scale posttensioned steel connections. J Struct Eng ASCE 131(3):438–448
- 35. Lin YC, Sause R, Ricles JM (2013) Seismic performance of a steel self-centering moment resisting frame: hybrid simulations under design basis earthquake. J Struct Eng ASCE 139 (11):1823–1832. https://doi.org/10.1061/(ASCE)ST.1943-541X.0000745

- 36. Lin YC, Sause R, Ricles JM (2013) Seismic performance of a large-scale steel self-centering moment resisting frame: MCE hybrid simulations and quasi-static pushover tests. J Struct Eng ASCE 139(7):1227-1236. https://doi.org/10.1061/(ASCE)ST.1943-541X.0000661
- 37. Garlock M, Sause R, Ricles J (2007) Behavior and design of post-tensioned steel frame systems. J Struct Eng ASCE 133(3):389-399
- 38. Ahmadi O, Ricles JM, Sause R (2018) Modeling and seismic collapse resistance study of a steel SC-MRF. Soil Dyn Earthq Eng 113:324–338. https://doi.org/10.1016/j.soildyn.2018.
- 39. Soong TT, Spencer BF Jr (2002) Supplemental energy dissipation: state-of-the-art and stateof-the-practice. Eng Struct 24(3):243-259
- 40. Christopoulos C, Filiatrault A (2006) Principles of passive supplemental damping and seismic isolation. IUSS Press, Pavia
- 41. ASCE (2007) Seismic rehabilitation of existing buildings. ASCE/SEI 41-06, Reston, VA
- 42. BSSC (2009) NEHRP recommended seismic provisions for new buildings and other structures. FEMA P-750 2009 Ed., Federal Emergency Management Agency, Washington, DC
- 43. ASCE (2017) Minimum design loads ad associated criteria for buildings and other structures. ASCE/SEI 7-16, Reston, VA
- 44. Pekcan G, Mander JB, Chen SS (1999) Fundamental considerations for the design of nonlinear viscous dampers. Earthq Eng Struct Dyn 28(11):1405-1425
- 45. Terenzi G (1999) Dynamics of SDOF systems with nonlinear viscous damping. J Eng Mech 125(8):956-963. https://doi.org/10.1061/(ASCE)0733-9399(1999)125:8(956)
- 46. Lin W, Chopra A (2003) Earthquake response of elastic single-degree-of-freedom systems with nonlinear viscoelastic dampers. J Eng Mech 129(6):597-606. https://doi.org/10.1061/ (ASCE)0733-9399(2003)129:6(597)
- 47. Sorace S, Terenzi G (2008) Seismic protection of frame structures by fluid viscous damped braces. J Struct Eng 134(1):45-55. https://doi.org/10.1061/(ASCE)0733-9445(2008)134:1 (45)
- 48. ASCE (2010) Minimum design loads for buildings and other structures. ASCE/SEI 7-10, Reston, VA
- 49. AISC (2010) Prequalified connections for special and intermediate steel moment frames for seismic applications. ANSI/AISC 358-10, Chicago
- 50. AISC (2010) Seismic provisions for structural steel buildings. ANSI/ AISC 341-10, Chicago
- 51. AISC (2010) Specification for structural steel buildings. ANSI/AISC 360-10, Chicago (2010)
- 52. Galambos TV, Ellingwood B (1986) Serviceability limit states: deflection. J Struct Eng 112 (1):67–84. https://doi.org/10.1061/(ASCE)0733-9445(1986)112:1(67)
- 53. Ellingwood BR (2001) Earthquake risk assessment of building structures. Reliab Eng Syst Saf 74(3):251-262
- 54. McCormick J, Aburano H, Ikenaga M, Nakashima M (2008) Permissible residual deformation levels for building structures considering both safety and human elements. In: Proceedings of the 14th world conference on earthquake engineering, china earthquake administration ministry of construction, Beijing
- 55. Chopra AK (2011) Dynamics of structures: Theory and applications to earthquake engineering, 4th edn. Prentice Hall, Upper Saddle River
- 56. Moehle J et al (2011) Case studies of the seismic performance of tall buildings designed by alternative means. Pacific Earthquake Engineering Research Center College of Engineering University of California, Berkeley PEER Report 2011/5
- 57. Smith RJ, Willford MR (2007) The damped outrigger concept for tall buildings. Struct Design Tall Spec Build 16:501-517

- 58. Al-Subaihawi S, Kolay C, Marullo T, Ricles JM, Quiel SE (2020) Assessment of wind-induced vibration mitigation in a tall building with damped outriggers using real-time hybrid simulations. Eng Struct 205:110044. https://doi.org/10.1016/j.engstruct.2019.110044
- ASCE (2005) Minimum design loads for buildings and other structures. ASCE/SEI 7-05, Reston, VA
- 60. Wan EA, Van Der Merwe R (2000) The unscented Kalman filter for nonlinear estimation. In: Proceedings of the IEEE 2000 adaptive systems for signal processing, communications, and control symposium 2000, pp 153–158
- 61. Ricles J, Kolay C, Marullo T (2021) HyCoM-3D: A Program for Multi-Hazard Nonlinear Dynamic Analysis and Real-Time Hybrid Simulation of 3-D Civil Infrastructure Systems (HyCoM-3D) User's Manual. ATLSS Report No. 20–02. Lehigh University, Bethlehem
- 62. Al-Subaihawi S (2022) Real-time hybrid simulation of complex structural systems. PhD Dissertation. Lehigh University, Bethlehem, PA